Chapter III

A Bubble Is Born (Nucleated): Microfluidic Flow Focusing Reveals Early Stages of Bubble Growth

> Time and space are modes by
> which we think and not conditions
> in which we live.
>
> Albert Einstein

The idea to use flow-focusing was first proposed by Prof. Julie Kornfield. The idea to perform flow-focusing with a capillary-based microfluidic device came from a chance lunch-time discussion with Prof. Stuart Prescott (UNSW, Australia). Dr. Orland Bateman led initial development of an acrylic-sheet microfluidic channel and assisted with the development of the final capillary-based design. Dr. Thomas Fitzgibbons (Dow) suggested the use of PEEK sleeves to maintain a high-pressure seal around the observation capillary. Dr. Valerie Scott was instrumental in loaning us the ISCO 260D high-pressure syringe pump from the Jet Propulsion Laboratory (NASA). Steve Weigand (Argonne) designed and set up the experiment to test the signal from SAXS.

While Chapter II focuses on the mother phase of polymer with dissolved CO_2, this Chapter and those that follow focus on the bubbles born by this mother phase upon reducing the pressure. If the pressure is reduced enough, bubbles may be born without the assistance of a surface by homogeneous nucleation, as discussed in Chapter I. Experimental measurements of homogeneous bubble nucleation in polymers have been limited by its stochasticity in space and time, its rapid depletion of dissolved gas, and the difficulty of eliminating heterogeneous nucleation, however. Here, we describe our experimental method for overcoming these challenges with a custom microfluidic channel and high-speed optical microscopy. To mitigate stochasticity in space, we localize supersaturation near the centerline of flow through a channel in a custom high-pressure (> 10 MPa) microfluidic flow-focusing apparatus. Due to the roughly linear decrease in pressure with distance from the inlet, there is a range of axial positions at which the supersaturation is sufficient to drive homogeneous bubble nucleation. We mitigate stochasticity in time by observing those positions where homogeneous nucleation occurs often enough to detect many bubbles (several per second) and rarely enough that bubbles can be studied individually. Previously, it was thought that the stochasticity of bubble nucleation posed a fundamental limitation that "[did] not lend itself [nucleation] to generating large amounts of reliable, tightly bunched data" [1]. Because the flow is continuously replenished, we can observe bubble nucleation at a specific degree of supersaturation for as long as desired (at least, for several hours), making possible the generation of such data and overcoming the challenge of rapid depletion of dissolved gas by homogeneous bubble nucleation. Finally, the apparatus isolates the nucleating stream within a sheath of pure polymer, which prevents heterogeneous nucleation along walls (although there is still a possibility of small particles in the nucleating stream).

Although we designed the microfluidic channel for compatibility with small-angle X-ray scattering (SAXS) and light scattering, we determined that high-speed optical microscopy would offer the richest data source; the possibilities of measuring bubble nucleation with SAXS and light scattering are discussed in Section III.S6 of the Supplementary Information. Due to the diffraction limit of light, optical microscopy can only detect the early growth of bubbles larger than about 1 μm, whereas nucleated bubbles may be as small as 10 nm. Therefore, the method described in this Chapter does not directly observe bubble nucleation. How we fit a model to the observable period of bubble growth and use it to extrapolate the growth backward in time to the moment of nucleation is discussed in Chapter V.

III.1 Studying Homogeneous Bubble Nucleation: Challenges and Solutions

Have you ever seen something just as it disappeared? A shooting star? A bolt of lightning? Short, stochastic events like these can be as frustrating as they are fascinating. Because they are stochastic, we do not know where and when to look; because they are sudden, they disappear as soon as we do.

Single-Shot Studies of Bubble Nucleation Are Cluttered and Tedious

Homogeneous bubble nucleation is one such short, stochastic event. Techniques with the spatial resolution to distinguish nanoscopic bubble nuclei, such as small-angle X-ray scattering (SAXS) [2] or scanning electron microscopy (SEM) [3–20], lack the time resolution to capture them live, only reporting measurements of bubbles in a solidified matrix. Techniques that could achieve sub-microsecond time resolution to capture the nucleation event, such as optical microscopy of batch foaming [3, 9, 11, 14, 19, 21–34], lack the spatial resolution to distinguish the nucleation event itself, only reporting micron-scale images of the early growth. As discussed in Section I.4, this dilemma has prevented direct experimental observation and quantification of homogeneous bubble nucleation, leaving us uncertain of the validity of the theoretical models available. The problem is further exacerbated by the rapid depletion of dissolved gas by homogeneous bubble nucleation relative to heterogeneous bubble nucleation due to the presence of nucleation throughout the bulk. Due to this challenge, measurements of homogeneous bubble nucleation in the literature are performed in batch processes and, therefore, require new sample preparation for each measurement, slowing down data acquisition. Measurement of homogeneous bubble nucleation also requires an exceptional degree of cleanliness and isolation from surfaces to prevent heterogeneous bubble nucleation from depleting the dissolved gas before homogeneous bubble nucleation is possible.

Nevertheless, given the challenges of direct observation, researchers have learned a tremendous amount about effects on bubble nucleation from indirect observations. Among the most common indirect observation methods is SEM analysis of the cell structure after foaming. While SEM achieves high spatial resolution, it is limited to analysis of the cells of the final solidified foam, using the number of cells as an estimate of the number of nucleation events despite the coalescence and ripening of bubbles during foaming. By counting cell number and size distribution of foams with SEM, researchers have elucidated how bubble nucleation is affected by photopolymerization [14], the addition of nucleant particles like talc [16], the rate of depressurization [15], wall effects [11], formulation [11], polymer glass transition temperature [4], polymer branching architecture [17], two-stage foaming [13], and polymer crystallization from the melt [7].

Other researchers have sought more direct observation at the expense of spatial resolution, observing the nucleation of bubbles upon depressurization of polymer–gas mixture in high-pressure cells with high-speed microscopy, which can capture bubble growth on the micron spatial resolution and millisecond time resolution. These batch foaming experiments, many of which were based on the apparatus designed by Guo *et al.* [21], have uncovered how bubble nucleation is affected by photopolymerization [14], depressurization rate [27], shear [29], extensional stretching [19, 20, 30], polymer crystallization [28, 30, 33], foaming agents (sodium bicarbonate [34], talc [19], and nano-clays [35]), temperature [33], physical blowing agent (*e.g.*, CO_2 [3, 9, 22, 24], N_2 [24], hydrocarbons like cyclopentane [3, 9], pentane [36], and isopentane [37], and alcohols [22]), wall effects [11], formulation [11], and melt retraction [25]. While microscopy studies are limited to a two-dimensional field of view by significant light scattering from bubble surfaces, a study by Perez-Tamarit *et al.* acquired three-dimensional scans of early bubble growth during polyurethane foaming with X-ray tomography at a synchrotron X-ray source, which they used to study the nucleating effect of nanoparticles [38]. Scattering likewise probes a three-dimensional volume of the foam and allows for the estimation of the bubble size distribution, as demonstrated with Mie scattering [39], diffusing wave spectroscopy [11], and small-angle X-ray scattering [2], but the latter typically requires too long of acquisition times (seconds) to study nucleation directly.

Although the studies above have provided tremendous insight into bubble nucleation in polymer foaming, they are performed in batches, often requiring a waiting period to dissolve CO_2 into a highly viscous polymer sample to prepare for foaming [40]. Ando *et al.* offered an elegant method for repeated homogeneous nucleation of bubbles by local heating with a laser [41]. The heated region nucleates a single bubble in the bulk and quickly returns to equilibrium afterward for another measurement. This technique has not been applied to polymer foams, however. Within the context of polymer foaming, Tsujimura *et al.*, and later, Taki *et al.*, developed transparent, high-pressure continuous flow cells for observing the onset of foaming of polymer–gas solutions as it flowed through a channel between two thinly spaced glass plates [27, 42, 43] or in an injection molding cell [44]. Because the foaming fluid is in contact with the glass plates, however, much of the nucleation was likely heterogeneous along the glass surfaces, leading to a non-uniform foaming front and preventing study of homogeneous bubble nucleation due to the higher level of supersaturation that it requires.

Turning Time into Space

Almost all the studies discussed above suffer from the same dilemma between time resolution and spatial resolution; those that do not suffer from parasitic heterogeneous nucleation. This dilemma only exists for short, stochastic patterns in time; in space, we can thoroughly scrutinize short (in length), stochastic patterns like Turing patterns and glasses as long as we want. Is there a way to map a time sequence onto space to permit thorough scrutiny as well?

Novice jazz musicians like myself have long grappled with the same problem, particularly when studying “bebop.” Only the most talented of musicians can decipher a "lick" from this style of mid-century jazz known for its rebelliously fast tempos and unpredictable patterns [45]. Record it onto a vinyl disk, however, and even the novice can pick out the notes by slowing down playback and looping each section in her quest to play like the pros; the sudden and stochastic becomes intelligible.

Such a mapping of time onto space naturally exists for heterogeneous bubble nucleation, for which bubbles are continuously nucleated at the nucleation site with little effect on the bulk concentration. The bubbles then rise at a predictable velocity due to their buoyancy, allowing the observer to correlate each position to a point in the bubble's lifetime (see Figure I.2b). On the contrary, homogeneous bubble nucleation quickly depletes the bulk of excess dissolved gas necessary for further nucleation.

At the turn of the millennium, the Austin group demonstrated how to put kinetics "on repeat" with a microfluidic technique they called "flow-focusing" [46, 47]. The technique flows a fluid stream of interest inside another fluid stream, often studying the kinetics of reactions occurring along their interfaces. Due to the microscopic dimensions of their channels, the Reynolds number Re remained in the laminar regime despite low viscosities and high speed, so the fluid flowed along straight streamlines and maintained a constant speed [48]. Constant flow speed allowed the researchers to correlate the time that particular portion of protein was in contact with the buffer to the distance it had traveled along the channel by dividing that distance by the speed. The researchers could then scrutinize each millisecond in the timeline of the protein-folding kinetics for long periods of time by observing the corresponding location along the length of the capillary, allowing for observation with techniques that require long exposure times, such as small-angle X-ray scattering (SAXS) [47]. The design of similar devices took off as the fabrication of precise microfluidic channels polydimethylsiloxane (PDMS) with photolithography became more widely available [49] due to its small sample-size requirements and laminar flow. Unlike the original devices produced by the Austin group, focused on generating an unperturbed interface between nearly identical fluids, many of the devices that followed considered unlike fluids with an interfacial tension, such as oil and water. Even a small amount of interfacial tension drives the rapid formation of droplets due to the Plateau–Rayleigh instability [48]. The resulting droplet-based devices permitted the observation of millisecond-scale kinetics of processes like gelation [50], enzymatic reaction[51], and ice nucleation [52], often leveraging the unique mixing behavior of droplets [53].

High-pressure Microfluidics

Due to the permeability of PDMS, experiments with these devices must be maintained near atmospheric pressure; an experiment performed at 50 psi is already considered “high pressure” [54]. The study of homogeneous bubble nucleation requires significantly higher pressures, however, both to achieve sufficient supersaturation and, in the case of polymer foams, to pump highly viscous fluids through microscopic channels. High-pressure microfluidics therefore faces its own dilemma: how does one design a design (1) strong enough to withstand high pressure (MPa-scale) and (2) transparent enough to allow optical observation? Glass and silicon became materials of choice due to their high pressure resistance (up to 40 MPa), compatibility with photolithography to etch precise microfluidic channels, and high optical transparency [55, 56]. To connect glass and silicon chips to laboratory devices while maintaining high pressures and small dead volumes, pressure-resistant connections from these chips to pumps and sampling devices were developed, some designing custom fittings [57, 58] and others adapting existing fittings [59]. To provide high pressure with precise flow control, these devices use high-pressure syringe pumps, such as those produced by Teledyne ISCO. Nevertheless, etching glass microfluidics requires a budget and resources not available outside dedicated microfluidics or photolithography labs.

An alternative, more accessible method for high-pressure microfluidics is capillary-based microfluidics, which flow fluids through capillary tubes instead of etched channels. Utada *et al.* initially pioneered the use of tapered microcapillaries to flow one fluid inside a sheath of another fluid, which we will refer to as “sheath flow” [60]. Marre *et al.* adapted this coflow microcapillary device to ensheath supercritical CO_2 with water at high pressure (8–18 MPa) [61], which was later modified to operate at higher temperatures and pressures [62]. Although the capillary walls are thin, the interior surface area is also smaller, reducing the force applied to the wall material, such that defect-free silica capillaries can withstand tens of MPa in pressure [63]. Leakage is most common at the connections between capillaries and other parts of the microfluidic device. Standard compression fittings such as Swagelok or VICI Valco fittings cannot be applied directly to silica due to its brittleness. Many methods for sealing these connections to withstand pressures over 10 MPa have been demonstrated in the literature, but most require irreversible chemical bonding [64, 65]. Some groups have achieved high pressure with removable fittings. Maharrey and Miller reached pressures as high as 28 MPa using HPLC stainless steel compression fittings on a quartz capillary ensheathed by a polyether ether ketone (PEEK) sleeve [66]. Luther and Braeuer reported a pressure tolerance of 8.5 MPa for a connection between fused silica capillary epoxied in a sleeve and a reusable stainless steel port-connector [63]. Chen-Jolly *et al.* demonstrated that high pressures can be maintained in flexible perfluoroalkoxy (PFA) tubing in a slightly larger, millimeter-scale device [67].

III.2 High-pressure Microfluidic Hydrodynamic Focusing Localizes Supersaturation in Space and Time

By combining concepts from flow-focusing and high-pressure capillary microfluidics, we developed a continuous-flow microfluidic channel to observe homogeneous nucleation and early growth of gas bubbles in the polymer during rapid depressurization from industrially Trelevant pressures (about 10 MPa). Unlike many other capillary-based flow-focusing devices in the literature, which flow unlike fluids and thus generate droplets [68, 69], we consider fluids with sufficiently low interfacial tension and with high enough viscosities to suppress the breakup of the inner stream into droplets. We begin with a discussion of how the design of the apparatus produces sheath flow, followed by a discussion of its implications for the pressure along the flow and its role in localizing bubble nucleation. We then describe our fabrication method and some of the limitations of the device that were overcome by a careful balance of the operational parameters. We close this chapter with a discussion of the high-speed optical microscopy setup with which we captured the early bubble growth, whose measurement and modeling we will discuss in Chapters IV and V, respectively.

Flow-focusing Principle

One of the primary motivations behind flow-focusing is to surround the flow of the fluid of interest with a sheath of another fluid, isolating it from the inner walls of the flow channel. The microfluidic dimensions of the channels maintain this “sheath flow” throughout the apparatus. A schematic of the apparatus, expected flow, and principle behind taking measurements is shown in Figure III.1. An example validation of sheath flow is shown in Figure III.S2.

In capillary-based flow focusing [63, 68, 69], sheath flow is produced inside a tee junction by enveloping a capillary that extends across the tee junction (the “inner capillary”) with the outer fluid before entering a transparent capillary for making

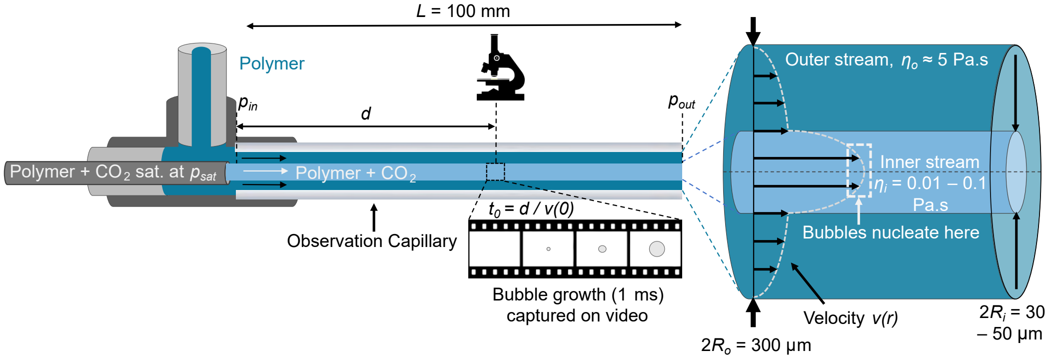

Figure III.1: Schematic of capillary microfluidic flow-focusing and flow profile for mapping timeline of kinetic process along length of a transparent capillary. Polymer with dissolved gas (CO_2) passes through a tee junction inside a narrow inner capillary to the entrance of the transparent observation capillary. Pure polymer enters through the top of the tee junction and ensheaths the inner stream before entering the observation capillary. Because of the high viscosities (up to 5 Pa.s) and narrow dimensions (300 μm inner diameter of observation capilary, 30–50 μm inner stream), the Reynolds number $Re < 10$, so the flow is laminar and the miscible inner and outer streams flow along straight streamlines with minimal mixing. On the right, the velocity profile predicted from Stokes flow is shown, with a higher velocity gradient in the inner stream due to the lower viscosity. Due to the loss of dissolved gas to the outer stream along the interface of the inner stream from diffusion, nucleation is most likely at the center, where the concentration of CO_2 is highest. The speed at the center $v(r = 0)$ is consistent and stable, so the time for a fluid element at the center to reach a distance d along the observation capillary is $t_0 = d/v(0)$. A microscope or other imaging device (eye schematic) can observe that location to watch the subsequent $\approx$ 1 ms of bubble growth immediately after t_0. By translating along the length L (100 mm), the average bubble behavior from the inlet pressure p_{in} to the outlet pressure p_{out} can be imaged. See Figure III.2 for the estimated pressure profile.

observations (the "observation capillary"), as shown schematically in Figure III.1. During operation of the instrument, a polymer–gas mixture flows from the left of the diagram through the inner capillary to the right end of the tee junction, where it exits the inner capillary near the entrance of the observation capillary. We considered mixtures of polyol and CO_2, but bubble nucleation could be studied in other viscous liquid–gas mixtures as well. Meanwhile, pure polymer flows from the top of the diagram around the inner capillary before flowing to the right into the observation capillary, where it ensheaths the polymer–gas mixture. At this point, the fluid pressure is p_{in}, which we kept at least 10% higher than the saturation pressure of the dissolved CO_2 p_{sat} to prevent heterogeneous bubble nucleation along the inside surface of the inner capillary. Once ensheathed, the inner stream is isolated from the inside surface of the observation capillary, preventing heterogeneous nucleation (unless a solid contaminant enters the flow—see the discussion of this problem in Chapter VI). This sheath flow continues 100 mm to the end of the observation capillary where it reaches the outlet pressure p_{out}, which we kept at atmospheric pressure. Unlike droplet-based microfluidics [53], the inner and outer streams here are miscible, having the same composition besides a small fraction of gas in the inner stream. Given that we will show that the flow is laminar as well, the interface between them remains unperturbed in the absence of bubbles, only diffusing a small amount of gas a few microns into the outer stream.

In comparison to many microfluidic devices, the inner diameter of our observation capillary is large (300 μm) and the flow speeds are fast (up to 1 m/s), but the flow remains laminar due to the high viscosity of the outer stream polymer and the narrow dimension of the inner stream (30–50 μm), as shown in the flow diagram on the right of Figure III.1. We show that the flow is laminar by estimating the Reynolds number for the inner and outer streams, which have different flow due to the significantly lower viscosity of the inner stream as a result of the dissolved CO_2. The Reynolds number is defined as $Re = \frac{\rho U L}{\eta}$ for fluid density ρ, speed U, length scale L, and viscosity η. For the outer stream, $\rho \approx 1000$ kg/m^3, $U < 0.5$ m/s, $L =$ 300 μm (ID of observation capillary), and $\eta \approx 5$ Pa.s (see polyol "1k5f" in Table II.1), yielding $Re < 0.1$, indicating Stokes flow ($Re \ll 1$). For the inner stream, $\rho \approx$ 1000 kg/m^3, $U \approx 1$ m/s, $L < 50$ μm, and $\eta > 0.01$ Pa.s, yielding $Re < 5$, indicating laminar ($Re \ll 2000$) but not Stokes flow. While the inner stream may not always be in the Stokes flow regime, we assume Stokes flow and note that the polymers are Newtonian (see Figure III.S1 in the SI for measurement of viscosity in a shear rate sweep) to estimate the velocity profile as a function of the radial coordinate $v(r)$. This velocity profile is depicted in Figure III.1 and is similar to Poiseuille flow with a steepened gradient at the center due to the lower viscosity; see Section III.S1 for the derivation. While the velocity gradient is steep near the surface of the inner stream, bubbles generally nucleate at the center of the inner stream, where the velocity gradient is smallest, due to the loss of CO_2 to the outer stream along the edges. Consequently, when we observe a bubble nucleate at the center of the stream, we can estimate the time since that fluid element entered the observation capillary by dividing the distance d from the entrance of the observation capillary by the velocity at the center stream $v(0)$, giving $t_0 = d/v(0)$. The distance along the capillary therefore maps directly onto the timeline of the flow. We then capture around 1 ms of the growth of the bubble on high-speed video as it travels along the field of view of our microscope, as discussed later in this Section. Once bubbles nucleate downstream, however, the viscosity drops significantly and the flow is no longer completely laminar.

Due to the small dimensions, the flow rates can be kept below 300 μL/min for the outer stream and 100 μL/min for the inner stream, such that a few hundred milliliters of fluid was sufficient for a full day of experiments.

Pressure

Relative to previous high-pressure capillary microfluidics [63], the fluid undergoes a steep pressure gradient along the observation capillary (about 100 MPa/m over 100 ms). This rapid rise in supersaturation of the dissolved gas drives a significant increase in the rate of homogeneous bubble nucleation over the range of our translation stage. Because of the high supersaturation required for homogeneous nucleation, we can set up experimental conditions under which bubbles do not nucleate before reaching the last third of the observation capillary. Most of the flow is thus bubble-free and, as discussed earlier, remains in or near the Stokes flow regime. Because the polymers are Newtonian (Section III.S1), we assume a roughly constant pressure gradient along most of the observation capillary, an example of which is shown in Figure III.2.

In this example experiment, CO_2 was dissolved into the polyol for the inner stream at a pressure of 7 MPa, just below the critical pressure (7.39 MPa [70]). The flow rates were chosen to keep the pressure at the inlet higher, p_{in} = 10 MPa, and prevent nucleation of bubbles along the walls of the inner capillary. Assuming a constant pressure gradient, we estimate the pressure profile with the plot in the lower half of the figure along the 100 mm length of the observation capillary. The polymer–CO_2 mixture remains below the saturation pressure for the first 30 mm, so no homogeneous bubble nucleation is observed. After, the pressure in the channel drops below the saturation pressure, supersaturating the solution. Because homogeneous nucleation requires high degrees of supersaturation, we do not observe bubbles until about 70 mm downstream, where the pressure is about 3 MPa. Within the field of view (about 1 mm), we observe a bubble grow to the width of the inner stream. The change in pressure during this growth is about 0.1 MPa, a decrease of about 3%, so we conclude that most of the growth is the result of the diffusion of CO_2 into the bubble rather than expansion of the gas due to the decreasing pressure (although we account for this change in pressure in our model of bubble growth in

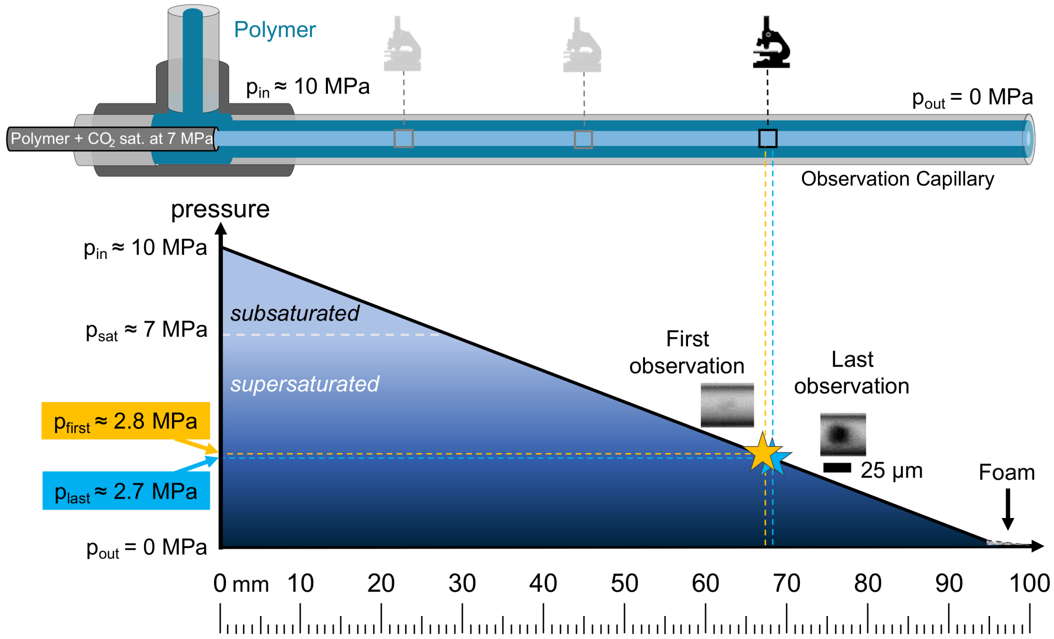

Figure III.2: Schematic of the pressure profile along the microfluidic capillary described in Figure III.1. In this example experiment, CO_2 is dissolved in polyol at a saturation pressure $p_{sat} = 7$ MPa. The inlet to the observation capillary is kept at a higher pressure ($p_{in} = 10$ MPa) to prevent heterogeneous bubble nucleation along the interior of the inner capillary before sheath flow. Because the fluids are Newtonian before bubbles nucleate (see Figure III.S1), we assume a constant pressure gradient. When a considerable number of bubbles has nucleated and produced a foam near the end of the capillary, the pressure gradient decreases signficantly and we can no longer assume Newtonian behavior. The estimated pressure profile is shown in the bottom plot. The fluid is subsaturated (light blue region) near the entrance of the observation capillary; bubbles are not observed (gray eye schematic). Once supersaturated (dark blue region), bubbles are not observed until reaching high supersaturation (black eye schematic), in this case, at $p_{first} = 3$ MPa (yellow star). The bubble can be observed over a field of view of about 1 mm, such that the pressure at the last observation has dropped only to $p_{last} = 2.9$ MPa (blue star). The distance along the observation capillary is shown at the bottom.

Chapter V). Near the end of the observation capillary, bubbles have grown large enough and nucleation is frequent enough that the inner stream becomes a foam. The location of this transition depends on the flow rates and concentration of CO_2 and can be varied anywhere along the observation capillary. Due to the significant reduction in viscosity upon foaming, we expect a significantly smaller pressure gradient here. This lower pressure gradient results in an error in our estimation of the internal pressure of the capillary. This error is usually on the order of only a few percent for most of the capillary, so we generally ignore this effect.

Device Fabrication

After exploring several designs to implement this flow-focusing principle (see Section III.S5 in the SI for their descriptions), we found the most success and simplicity with a design based on a tee junction machined out of a block of acrylic (see Figure III.S4 in the SI for dimensions). A digital image of the instrument built with this design mounted in a red, 3D-printed polylactic acid (PLA) case is shown in Figure III.3. The image at the top shows the inner and outer streams entering through stainless steel tubing (Restek 316 stainless steel tubing #27768, 1/16" OD, 0.040" ID) into the acrylic tee junction and meeting just before (to the left of) the entrance of the observation capillary (outlined in a white solid line). Due to the high viscosity of the outer stream, we did not insert the inner stream capillary into the observation capillary, as is done in some capillary devices for a more robust sheath [68, 69], which would have added significant pressure resistance at the entrance of the observation capillary. Rather, we extended the inner stream tubing with a small capillary (800 μm OD, 500 μm ID, Cynken #CKS1824, 304 stainless steel) that spanned across the entrance of the outer stream up to 1 mm from the entrance of the observation capillary, which we attached with silver epoxy. While the inner stream flowed slightly off center (see example snapshots in Figure III.3 due to the imprecision of this technique and the one-sided flow from the outer stream (better designs include flow from two sides [47] but require an additional pump), it was simple to assemble.

To withstand the high pressures inside the acrylic tee junction (up to 15 MPa), we connected the tubing to the tee junction with VICI Valco nuts and ferrules (316 stainless steel, 1/16", nuts #ZN1-10, and ferrules #ZF1S6-10). While they are rated to 10,000 psi (about 70 MPa) when used in stainless steel fittings, they permitted a gradual leak after about an hour of 10 MPa flow in the acrylic tee junction. This leak could have been prevented by epoxying the fittings into the acrylic, albeit at the expense of removability. Although the acrylic tee junction tolerated the high pressure as well, it showed some cloudiness from stress (seen faintly along its internal channels in Figure III.3). Additionally, the outer stream eventually indented a small cusp in the opposing wall (not seen in Figure III.3). We did not observe any effects on the flow as a result of these changes, however.

Because the observation capillary was too brittle to apply the VICI Valco ferrule directly, we inserted it into a hollowed-out extreme-pressure PEEK sleeve (McMaster Carr #51085K48, 1/16" OD, 0.03" ID) before applying the ferrule.

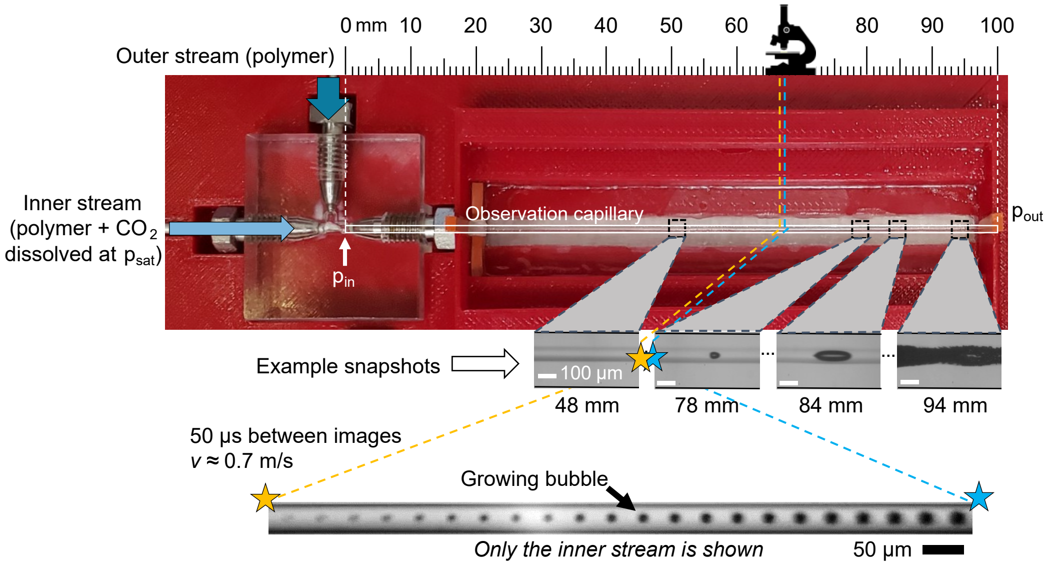

Figure III.3: Image of custom microfluidic capillary and acrylic tee junction in red 3D-printed microscope mount. A polymer–CO$_2$ mixture saturated at pressure p_{sat} enters from the left (light blue arrow) and travels through a narrow inner capillary to the entrance of the observation capillary (outlined in white). Pure polymer enters through the top (dark blue arrow) and ensheaths the inner capillary and inner stream of polymer–CO$_2$. This sheath flow enters the 100 mm observation capillary at pressure $p_{in} > p_{sat}$ and exits at p_{out}, atmospheric pressure. Behind the observation capillary is a transparent acrylic sheet that forms the base of an oil reservoir that reduces lensing from the curved surfaces of the observation capillary. The edges of the reservoir are sealed with orange silicone rubber at the left and right ends of the observation capillary. Micrographs taken at different points along the observation capillary (corresponding to different times and pressures) are shown below the image, showing how the inner stream (48 mm) nucleates bubbles (78 mm) that grow (84 mm) and ultimately generate a foam (94 mm). A set of collated images of bubble growth captured with a high-speed microscopy between 67 (yellow star) and 68 mm (blue star) is shown at the bottom (inner stream only).

While the literature recommends epoxying this PEEK sleeve onto the capillary [63, 71], we did not find epoxy necessary if the sleeve fit snugly, *i.e.* if the PEEK sleeve did not slide when the capillary was held vertically. Even with the PEEK sleeve, other compression fittings like Swagelok apply too much compression and fracture the capillary. The VICI Valco ferrule is unique in that it has a rim along the interior of the thinner end that “chomps” into the PEEK sleeve, providing a pressure-resistant fitting with less strain on the capillary. A similar technique has been used to observe underwater microbes at pressures relevant to the bottom of the ocean [71].

The observation capillary must withstand high internal pressure (up to 15

MPa) and light handling and have high optical transparency. We considered borosilicate (Pyrex) and fused quartz due to their optical transparency, high flexural and tensile strength, and the availability of precision-manufactured capillaries. We successfully performed foaming experiments with an inexpensive borosilicate (Pyrex) observation capillary (Friedrich & Dimmock, Inc. #B100-50-100, ID = 500 μm, OD = 1000 μm); see Section III.S4 of the SI for estimation of the pressure ratings of these capillaries. Nevertheless, maintaining flow speeds near our target of 1 m/s under common operating conditions was easier with an inner diameter of 300 μm. We could only find fused quartz capillaries at that dimension (Molex #TSNC3001000/100, 300 μm ID, 1000 μm OD), although at almost one hundred times the cost, so we used them for the experiments discussed in this manuscript. Fused quartz also allows for compatibility with both X-ray scattering, because it is relatively featureless in the SAXS regime, and near-infrared imaging, due to reasonable transmission of wavelengths up to 3000 nm. We also tested PFA tubing for the observation capillary but found that it was too cloudy for precise optical measurement.

While the observation capillary is optically transparent, its curved inner and outer surfaces sharply refract much of the transmitted light, leaving all but the center portion of the flow dark. To prevent the refraction that causes lensing, index-matched material must fill in the curved surface such that light only passes between media of different indices of refraction orthogonal to the interface. The polyols tested (see Table II.1) have indices of refraction between 1.46–1.48, similar to the index of refraction of both borosilicate (1.47) and fused quartz (1.46). Therefore, the outer stream fluid will prevent lensing from the inner surface of the capillary. To prevent lensing from the outer surface, we submerge the observation capillary in Wesson vegetable oil, often used to turn borosilicate test tubes “invisible” due to its identical index of refraction (1.47) [72]. In Figure III.3, the oil (not shown) is contained in a reservoir between the orange strips of silicone rubber seen near the ends of the observation capillary and above a thin sheet of acrylic sealed with epoxy (not visible). Because the small silicone rubber seals at the extreme ends of the observation capillary are removable, they slowly leak oil, so oil must be replenished periodically during experiments. Refilling a reservoir with vegetable oil can be messy and tedious, so we also developed a technique for encasing the observation capillary in a square capillary filled with UV-cured optical adhesive (146H Norland optical adhesive, Edmund Optics #12-864), which we describe in Section III.S5 of the SI. This technique was prone to entrapping bubbles in optical adhesive before curing and the accumulation of optical artifacts on the exterior of the square capillary, so we preferred the oil bath.

The red plastic mount for the microfluidic channel in Figure III.3 was 3D-printed from PLA using a CraftBot 3D printer at the Caltech Sherman Fairchild Library's TechLab. CAD designs can be found in the accompanying data in `data/3_bubble_birth/device_design/mf_mount.stl`. The bottom of the mount was designed to fit snugly around the translating fixture on the microscope translation stage (Zeiss #473356-9901). For added stability, the mount contains four cubbies along the location of this metallic fixture for 8 mm × 8 mm × 8 mm NdFeB magnets to provide a magnetic connection. A long ramp at the outlet of the observation capillary funnels waste away from the outlet into a waste container beyond the translation stage.

At four distances along the observation capillary, snapshots of the flow taken with high-speed optical microscopy are shown marked with their distance from the inlet. In each case, the inner walls of the observation capillary are highlighted with a solid black line. The inner stream of polymer–CO_2 is clearly visible due to the lower index of refraction than the pure polymer outer stream, which causes a slight lensing effect. Farther along the capillary, the flow transitions from laminar (48 mm) to rare bubble nucleation (78 mm) to elongated bubbles (84 mm) to frequent nucleation and flow instabilities (94 mm). Within the field of view of the microscope of about 1 mm, we can watch the early growth of just-nucleated bubbles, an example of which is shown around 67 mm at the bottom of the figure (only the inner stream is shown). The first and last images are the same as those shown for the first and last bubble observations shown in Figure III.2.

Not shown in Figure III.3 are the two high-pressure syringe pumps, Teledyne ISCO 100DM and ISCO 260D, which pumped the inner and outer streams, respectively. These pumps had enough capacity for hours of continuous operation at 50 μL/min and 300 μL/min (ISCO 100DM: 103 mL, ISCO 260D: 266 mL), provided precise, pulseless flow (ISCO 100DM: 0.3% of setpoint, ISCO 260D: 0.5% of setpoint), and were rated to pressures well beyond our requirements (ISCO 100DM: 69.5 MPa, ISCO 260D: 51.7 MPa). We connected these pumps to 1/16" ball valves (Swagelok #SS-41GS2) with rigid 304 stainless steel extreme-pressure tubing (McMaster Carr #51755K11) connected to the pumps by an internal reducing ferrule and nut (Valco Instruments #IZR21T). The rigid tubing could break from too much flexing, so we stabilized those connections with steel clamps. We filled the ISCO 260D with pure polymer through wider, 3/32” inner diameter, 1/8” outer diameter nylon tube (Grainger #2VKT5) connected to the pump by a 1/8” ball valve (Swagelok #SS-41GS2), a high-pressure 1/8” OD tube (FreelinWade #1A-280-10, 0.073” ID), and 1/8” VICI Valco fitting (Valco Instruments, ferrule #ZF2S6-10 and nut #ZN2-10). The wider inner diameter was chosen to permit a faster refill rate of the viscous outer-stream polymer (“1k5f” in Table II.1).

While the pumps are expensive and the machining of the acrylic block must be precise, this microfluidic flow-focusing device offers a uniquely modular design allowing for use with a variety of different pumps, fluids, and observation capillaries to find the best for a given application.

Limitations

While this apparatus can provide unprecedented time resolution in measurements of early bubble growth in polymer foams, these design choices come at a cost that limits its measurement capabilities. Like all apparatuses, this apparatus operates best in a particular parameter range, which is discussed in greater depth in Section III.S2 of the SI. Outside this parameter range, certain assumptions about the flow are no longer valid. For example, if the viscosity difference between the inner and outer streams is too high, the interface may become unstable, as demonstrated in Section VIII.4. If the flow is too slow, whether due to high viscosity, a narrow observation capillary, or a low flow rate, the gas dissolved in the inner stream will diffuse into the outer stream, leading to a heterogeneous and low concentration profile of gas near the exit, where bubbles tend to nucleate.

Even inside the optimal parameter range, the apparatus does not always provide steady, consistent flow. As large bubbles grow and exit the observation capillary, they alter the effective length over which the pressure decreases to the outlet pressure because they cannot sustain a pressure gradient. These fluctuations in the pressure have little effect on the flow near the entrance, but near the exit, they can dramatically alter the local pressure and, consequently, the bubble nucleation and growth rates. The fluctuations can be so large near the exit that they can drive sudden, large-scale nucleation events, as shown in Figure VIII.S2. The limitations on the size of the inner stream (see Section III.S2 in the SI) place a fixed maximum size to which a bubble can grow before it is perturbed by the outer stream. Bubble growth measurements beyond this size no longer represent growth in an isotropic medium. When bubbles grow beyond this size, they elongate, speed up, and generate significant convective currents along their sides and behind their tails, producing a wake that affects the growth of bubbles within it, as discussed in Section VIII.2. Near the exit, enough bubbles growth to a large enough size that they overlap and interact strongly, leading to complex behavior and flow instabilities. At this point in the observation capillary, much of the surrounding fluid is depleted of CO_2 by bubbles or by diffusion into the outer stream. Additionally, the large number and sizes of bubbles often results in bubble–bubble interactions, opacity of the inner stream, and uncertainty in our estimation of the internal pressure. For these reasons, we exclude these measurements from our discussions of bubble nucleation and growth.

III.3 High-speed Optical Microscopy Captures Early Bubble Growth

Initially, we intended to detect bubble nucleation directly with small-angle X-ray scattering (SAXS), which detects features on the scale of bubble nucleation (1–100 nm) [73], and light scattering, which can detect features much smaller than the wavelength of the scattered light [74]. We estimated the signal we would detect using SAXS by measuring the signal-to-noise ratio from various concentrations of nanoparticle solutions, but found that the signal from bubble nucleation in our apparatus would likely be too faint for reliable estimation of the nucleation rate, which we discuss in Section III.S6 of the SI. Light scattering could provide a signal for sub-micron bubble nuclei, but because the difference in index of refraction between the inner and outer stream would distort the scattering pattern from the bubble, we were not confident that we could accurately measure the object size or distinguish bubbles from debris; our suggestions for a light-scattering experiment to count the frequency of bubbles is discussed in Section III.S6 in the SI. We instead chose to use high-speed optical microscopy to capture the early bubble growth. Because optical microscopy is limited by the diffraction limit of light, it cannot detect bubble nucleation. Nevertheless, it can capture images of the early growth with high time resolution (20–50 μs), which we use to extrapolate the nucleation time with a model of bubble growth in Chapter V. Here, we describe the high-speed optical setup we developed to capture these images.

Microscope

We used a Zeiss optical microscope with a revolving nosepiece and objective lenses with magnifications of 4x, 10x, and 20x. See Table III.1 for their properties.

We found that these lenses allowed us to observe coarsely over a large field of view (4x) and finely over a small field of view (20x). Lower magnification

Magnification	NA	Res. @ 550 nm [μm]	WD [μm]	Corrections
4x	0.10	2.75	55.5	Plan
10x	0.22	1.25	10	None
20x	0.40	0.69	5.8	MSPlan ULWD

Table III.1: Table of properties of the objective lenses used in this study, classified by magnification. NA is the numerical aperture. Res. @ 550 nm is the spatial resolution of 550 nm light. WD is the working distance. “ULWD” stands for ultra-long working distance.

would likely be unable to discern bubbles narrower than the inner stream, and higher magnification would not be able to span the entire inner stream (and would have too small a working distance and depth of field to capture bubbles in focus). We used a translation stage (Zeiss, #473356-9901) to translate the microfluidic channel for viewing different points along the observation capillary. A condenser with an adjustable aperture (Zeiss, #465267) allowed us to balance brightness and contrast depending on the numerical apertures of the different objectives. The light source was collimated below the microscope and reflected upward through a field diaphragm before reaching the condenser.

Lighting

The key to successful high-speed imaging is bright, steady lighting. Bright lights are plentiful, but most rely on the high power provided by power outlets. Because this electricity is AC, the resulting light flickers noticeably under high-speed imaging. Until recently, halogen lamps powered by high-voltage DC power supplies provided the brightest, most stable microscope light sources. Due to their low cost, we began this project using such a light source, powering a 400 W halogen lamp (Osram HLX Xenophot EVD 36 V 400 W #64663) with a 30 V, 10 A power source purchased from eBay. At full power (400 W), this light was advertised to reach a brightness of 16 kilolumens (klm). Because we operated the light at about 80% power with our limited power source, we expect it produced a brightness of about 12 klm, most of which was radiated in directions not captured by the microscope. Furthermore, the halogen light source grew dangerously hot after extended use.

Nowadays, LED light sources provide brighter light with less heat than halogen sources, though they cost significantly more. For the experiments presented in this manuscript, we used a 3.3 W, 70 klm LED (ThorLabs, cool-white SOLIS-1C), which never caused a heat hazard. Its brightness could damage the eye, however, so we covered all eyepieces during experimentation and wore tinted safety glasses while adjusting the lighting.

High-speed Camera

When purchasing a high-speed camera, the best camera provides a high-quality image with a high record rate and short transfer time. A high-quality image detects images over a high dynamic range with minimal readout noise. In light-starved applications, the dynamic range is best utilized by sensitive CMOS sensors with a high quantum efficiency (electrons generated per incident photon). A high record rate includes both a high frame rate and a high pixel count, and is measured in frames per second at 1 MP resolution. For a short transfer time, current state-of-the-art high-speed cameras use 10 Gb/s ethernet cables, either directly to a hard drive or connected through a Thunderbolt adapter—USB is not fast enough. The transfer protocol can usually be optimized significantly through adjustments to the software settings.

To accomplish these goals, we used a Photron Nova S6 (6400 fps @ 1 MP, 64 GB). This camera also allowed us to reach sub-microsecond exposures for use with the 20x objective, for which each pixel spanned less than 1 μm. While the camera recorded in 12-bit images, we typically compressed to 8-bit images for use with standard 8-bit image-processing methods (see Chapter IV for further discussion).

Experimental Setup

Briefly, we describe our procedure for saturating the polymer with CO_2 at high pressure, transferring the polymer–CO_2 mixture to a high-pressure syringe pump, and flowing the mixture through our high-pressure flow-focusing channel to drive bubble nucleation in the observation capillary.

First, slowly pour the desired polyol into the Teflon cup of a Parr reactor (Parr Instrument Company, #4760, 240 mL capacity), careful not to entrain bubbles. Mix in desired additives (*e.g.*, cyclopentane, surfactant—see Chapter VII). Seal Parr reactor top with 35 ft-lbs of torque, applied in three stages to the six bolts in a star-shaped pattern; if flammability is a concern, run a low-pressure flow of N_2 gas through the gas sampling valve until sealed. The Parr reactor is mixed with a brushless impeller at 5–10 RPM, which has been found to be slow enough not to entrain bubbles [3]. Gradually pressurize the Parr reactor by pumping CO_2 through the liquid sampling valve with an ISCO pump. Once the Parr reactor reaches the desired pressure or slightly higher, close the liquid sampling valve and let mix overnight, pumping in more CO_2 as needed.

Once the Parr reactor has equilibrated at the desired pressure, transfer its contents to the ISCO 100DM syringe pump through the liquid sampling valve. Throughout the transfer, the fluid must be kept above the saturation pressure to prevent bubble nucleation along the walls of the tubing. To pressurize the Parr reactor further, connect an N_2 gas tank (Airgas Industrial grade) equipped with a pressure regulator (Airgas CGA-580, 0–2500 psi #Y11N115H580-AG) to the gas sampling valve of the Parr reactor and increase the pressure by at least 100 psi (0.7 MPa). Because N_2 has a much lower solubility in polyol than CO_2 [75, 76], we assume that the additional partial pressure of N_2 will have a negligible effect on bubble nucleation. Before transferring the fluid to the ISCO 100DM, prime the tubing between the liquid sampling valve and the ISCO 100DM with pure polyol to maintain the pressure upon opening the valve. Next, open the liquid sampling valve and slowly fill the ISCO 100DM with the fluid, maintaining the pressure in the headspace with the N_2 pressure regulator. Once the ISCO pump has been filled with the desired amount of fluid, close its valve and the liquid sampling valve of the Parr reactor. Slowly depressurize the tubing between the Parr and the ISCO and between the N_2 cylinder and the Parr.

To perform the experiment, mount the microfluidic apparatus into the 3D-printed mount (see Figure III.3) and seal the ends of the oil reservoir with silicone rubber. Mount to the microscope translation stage with NdFeB magnets. Fill the oil reservoir with enough index-matched oil (Wesson vegetable oil) to submerge the observation capillary. Connect the ISCO 100DM pump (filled with the polyol–CO_2 mixture) to the inner stream tubing and the ISCO 260D (filled with the "1k5f" polyol—see Table II.1) to the outer stream tubing on the microfluidic apparatus. Prime and pressurize the apparatus and tubing with the ISCO 260D. Once the pressure in the tubing has reached the pressure in the ISCO 100DM, begin pumping the ISCO 100DM to provide the inner stream of nucleating fluid. After the inner stream forms in the observation capillary, adjust the flow until bubbles can be seen at the exit. Be careful not to let the pressure decrease so much that the entire apparatus fills with foam and depressurizes the ISCO 100DM. Different moments in the lifetime of the foaming flow can be captured by translating along the observation capillary.

With sufficient dissolved CO_2 and careful observation in the appropriate region of the observation capillary, we can capture the growth of bubbles immediately after they can be detected by optical microscopy, as seen in the image at the bottom of Figure III.3. To our knowledge, no other group has captured the growth following homogeneous bubble nucleation from a polymer–gas mixture with comparable time resolution (compare $\sim$ 20 *mu*s intervals between frames to the 20 ms intervals reported in Leung *et al.* [77]). Given that much of the nucleation in polymer foams occurs through homogeneous nucleation, we expect these data can help answer many unanswered questions in the field of polymer foaming, such as the wide variability in model estimates of the nucleation barrier (see discussion of the state of the literature in Section I.4).

III.4 Recommendations for Future Work

Our exploration of the capabilities of the instrument discussed in this Chapter has only been partial. Many improvements remain to be made, and many features have yet to be utilized. Here, we offer suggestions for both.

Improvements to Current Instrument

While the instrument successfully ensheaths in the inner stream with the outer, the inner stream does not run perfectly along the center of the observation capillary, as seen in the example snapshots in Figure III.3. The imprecision of the alignment of the smaller capillary silver-epoxied inside the inner stream tubing to extend it is one likely cause. We expect that the asymmetry of the tee junction, which receives the outer stream from only one side, also nudges the inner stream off center. A simple improvement might be to 3D-print a mount to align the smaller inner capillary inside the inner stream tubing while the silver epoxy is curing. If centering the inner stream is of high importance, a more invested researcher could machine an acrylic junction with symmetric inlets for the outer stream, both having the same length of tubing and fed by the same source.

The instrument in its current form also does not allow observation of the entire length of the observation capillary. While some obstruction of the entrance by the high-pressure fitting is inevitable, the region near the exit need not be obstructed. In the current iteration of the instrument, silicone rubber pieces are necessary at the ends of the observation capillary to slow leakage of the oil reservoir that reduces lensing. If done properly, the observation capillary can be encased in UV-cured optical adhesive (*e.g.*, Norland #146H) within a square capillary up just a few millimeters from the exit, as described in greater detail in Section III.S5 of the SI. The exit could then be supported on top of a transparent sheet before reaching the incline to the waste, which would allow observation at and beyond the exit of the capillary. Fractionally, most of the pressure quench occurs in the final few millimeters before the exit of the observation capillary, so we expect significant foaming. Although we explored this modification to the instrument, we did not implement it because of the difficulty of discerning the size and shape of such tightly packed bubbles. Future studies of the behavior of the fluid near atmospheric pressure should also consider alternative observation techniques.

Additional Features to Consider

The initial motivation of the present study was the nucleation and growth of bubbles in high-pressure polyurethane foaming. We focused on only one aspect of polyurethane foaming, the pressure quench, but the unique properties of polyurethane foam depend on the effects of the chemical reaction between isocyanate and polyol and the heat this exothermic reaction releases as well. To study the reaction of isocyanate with polyol, the inner stream could be replaced with isocyanate (*e.g.*, pMDI) and the reaction along its interface observed. From the observations of the advancing reaction front by Machuga *et al.* [78], we expect that a thread of isocyanate within a sheath of polyol could be completely penetrated by polyol within common residence times in the observation capillary ($\approx$ 100 ms). Another embodiment could first impinge the polyol and isocyanate streams in a tee junction at high pressure, as in industrial foaming nozzles [79]. The outlet of this tee junction would provide the inner stream for the tee junction in the current embodiment of the device, which would ensheath the reacting mixture with more polyol. For a diagram of how such a device with two flow-focusing tee junctions could be produced, see Figure 1 in the work of Hessberger *et al.* [68]. If the flow is fast enough, the reacting mixture could be ensheathed before causing fouling in the first tee junction the current embodiment. Isocyanate adds two additional challenges, however: (1) fouling and (2) exposure hazard.

The instrument presented in this Chapter is well suited to manage the first, fouling. First, the inner stream is completely isolated from the walls of the acrylic tee junction and observation capillary by the outer stream of polyol. Should some solid particles enter or form within the inner stream, they would be quickly flushed out by the overwhelming flow of the outer stream. Fouling may still occur along the walls of the tubing and inner capillary. In this case, they are both inexpensive and not too difficult to assemble, so the fouled part can be replaced. Pumping isocyanate directly with an ISCO pump is not recommended due to the difficulty of cleaning the interior in the case of following and high cost of repair. Instead, isocyanate could be pumped from a tubular reactor with a piston driven by hydraulic fluid from another pump, as shown for providing pressure in the waste stream in the apparatus of Chen-Jolly *et al.* [67]. The piston in the tubular reactor would isolate the isocyanate from the pump and could be more easily cleaned in the case of fouling.

The instrument in its present form is not as well suited to managing the chemical hazards of isocyanate due to the open-air waste collection. If isocyanate is used as the inner stream, the experiment will ideally be performed in a chemical hood, or at minimum, under a snorkel/elephant trunk in a well-ventilated environment. The small volumes and significantly larger quantity of outer stream fluid than inner stream fluid would reduce the likelihood of exposure to or inhalation of isocyanate, but the severity of isocyanate exposure should not be taken lightly.

The study of the effect of temperature on bubble nucleation with the present instrument would be interesting scientifically, but less practically relevant to polyurethane foam. By studying the effect of temperature on the nucleation rate at a fixed degree of supersaturation, the nucleation energy barrier can be estimated using the second nucleation theorem [80, 81], which could be directly compared to theoretical models, as discussed in Chapter VI. The polyurethane reaction heats up slowly, increasing by only a few degrees Celsius before the cream time (usually around 1 minute) [9]. Consequently, we do not expect a significant increase in the temperature in industrial polyurethane foaming within the residence time of the present instrument. Temperature does provide an additional control of supersaturation, as seen by its significant effect on CO_2 solubility in Section II.2, and it can be controlled more precisely than the pressure. For example, bubbles could be nucleated on demand by local heating of the inner stream fluid by a laser, as in the study of homogeneous bubble nucleation in water by Ando *et al.* [41]. In this way, bubbles could be nucleated at precise locations upstream of the field of view of the microscope to capture precise periods of their growth. Bubbles could also be nucleated in rapid succession to study their interaction along the inner stream. Additionally, to prevent bubble nucleation upstream of the observation capillary, the inner stream fluid can be chilled with the cold water bath feature of the ISCO 100DM, maintaining the fluid well below saturation. The oil reservoir used to reduce lensing could be heated to supersaturate the fluid, even beyond the degree possible with depressurization.

While only briefly explored in Chapter VII, the present instrument is well suited for studies of bubble nucleation from formulations of polyols, including physical blowing agents like cyclopentane and surfactants. These additives and others can be mixed with the polyol before dissolving CO_2 to explore their effect on bubble nucleation and foaming.

References

1. Lubetkin, S. D. Why Is It Much Easier To Nucleate Gas Bubbles than Theory Predicts? *Langmuir* **19,** 2575–2587. `https://pubs.acs.org/doi/abs/10.1021/la0266381` (2003).

2. Terekhov, A. Y. *et al.* Small-angle X-ray scattering measurements of helium-bubble formation in borosilicate glass. *Journal of Applied Crystallography* **39,** 647–651. ISSN: 0021-8898. `http://scripts.iucr.org/cgi-bin/paper?S0021889806025672` (Oct. 2006).

3. Brondi, C., Di Maio, E., Bertucelli, L., Parenti, V. & Mosciatti, T. Competing bubble formation mechanisms in rigid polyurethane foaming. *Polymer* **228,** 123877. ISSN: 00323861. `https://doi.org/10.1016/j.polymer.2021.123877%20https://linkinghub.elsevier.com/retrieve/pii/S0032386121005000` (July 2021).

4. Costeux, S., Khan, I., Bunker, S. P. & Jeon, H. K. Experimental study and modeling of nanofoams formation from single phase acrylic copolymers. *Journal of Cellular Plastics* **51,** 197–221 (2015).

5. Doroudiani, S., Park, C. B. & Kortschot, M. T. Effect of the crystallinity and morphology on the microcellular foam structure of semicrystalline polymers. *Polymer Engineering and Science* **36,** 2645–2662. ISSN: 00323888 (1996).

6. Forest, C., Chaumont, P., Cassagnau, P., Swoboda, B. & Sonntag, P. Polymer nano-foams for insulating applications prepared from CO2 foaming. *Progress in Polymer Science* **41,** 122–145. ISSN: 00796700. `https://www.sciencedirect.com/science/article/pii/S0079670014000689%20https://linkinghub.elsevier.com/retrieve/pii/S0079670014000689` (Feb. 2015).

7. Fu, L. *et al.* Improved cell nucleating effect of partially melted crystal structure to enhance the microcellular foaming and impact properties of isotactic polypropylene. *The Journal of Supercritical Fluids* **160,** 104794. ISSN: 08968446. `https://doi.org/10.1016/j.supflu.2020.104794%20https://linkinghub.elsevier.com/retrieve/pii/S0896844620300450` (June 2020).

8. Krause, B. *et al.* Ultralow-k Dielectrics Made by Supercritical Foaming of Thin Polymer Films. *Advanced Materials* **14,** 1041. ISSN: 09359648 (Aug. 2002).

9. Minogue, E. *An in-situ study of the nucleation process of polyurethane rigid foam formation* PhD thesis (Dublin City University, 2000), 1–194. `http://doras.dcu.ie/19076/`.

10. Park, C. B. & Cheung, L. K. A study of cell nucleation in the extrusion of polypropylene foams. *Polymer Engineering and Science* **37,** 1–10. ISSN: 00323888 (1997).

11. Roberts, C. *et al.* Bubblescale observations of polyurethane foam expansion. *AIChE Journal* **68,** e17595. ISSN: 0001-1541. `https://onlinelibrary.wiley.com/doi/10.1002/aic.17595` (May 2022).

12. Rizvi, A. & Park, C. B. Dispersed polypropylene fibrils improve the foaming ability of a polyethylene matrix. *Polymer* **55,** 4199–4205. ISSN: 00323861. `http://dx.doi.org/10.1016/j.polymer.2014.06.014` (2014).

13. Rizvi, A., Chu, R. K. M. & Park, C. B. Scalable Fabrication of Thermally Insulating Mechanically Resilient Hierarchically Porous Polymer Foams. *ACS Applied Materials & Interfaces* **10,** 38410–38417. ISSN: 1944-8244. `https://pubs.acs.org/doi/10.1021/acsami.8b11375` (Nov. 2018).

14. Taki, K. & Okumura, S. Production of Porous Polymeric Films with Unimodal or Bimodal Pore-Size Distributions via Depressurization- and Photopolymerization-Induced Bubble Nucleation in Low-Viscosity UV-Curable Monomer/High-Pressure CO2 Solutions. *Macromolecules* **43,** 9899–9907. `http://pubs.acs.org/doi/abs/10.1021/ma101748c` (Dec. 2010).

15. Tammaro, D., Iannace, S. & Di Maio, E. Insight into bubble nucleation at high-pressure drop rate. *Journal of Cellular Plastics* **53,** 551–560. ISSN: 0021-955X. `http://journals.sagepub.com/doi/10.1177/0021955X17695094` (Sept. 2017).

16. Tammaro, D. & Di Maio, E. Early bubble coalescence in thermoplastic foaming. *Materials Letters* **228,** 459–462. ISSN: 0167-577X. `https://www.sciencedirect.com/science/article/pii/S0167577X18309637` (Oct. 2018).

17. Wang, K. *et al.* A new strategy for preparation of long-chain branched polypropylene via reactive extrusion with supercritical CO2 designed for an improved foaming approach. *Journal of Materials Science* **51,** 2705–2715. ISSN: 0022-2461. `http://link.springer.com/10.1007/s10853-015-9584-x` (Mar. 2016).

18. Wang, G. *et al.* Role of elastic strain energy in cell nucleation of polymer foaming and its application for fabricating sub-microcellular TPU microfilms. *Polymer* **119,** 28–39. ISSN: 00323861. `http://dx.doi.org/10.1016/j.polymer.2017.05.016` (2017).

19. Wong, A., Chu, R. K., Leung, S. N., Park, C. B. & Zong, J. H. A batch foaming visualization system with extensional stress-inducing ability. *Chemical Engineering Science* **66,** 55–63. ISSN: 00092509. http://dx.doi.org/10.1016/j.ces.2010.09.038%20https://linkinghub.elsevier.com/retrieve/pii/S0009250910005841 (Jan. 2011).

20. Zhao, J., Wang, G., Zhang, A., Zhao, G. & Park, C. B. Nanocellular TPU composite foams achieved by stretch-assisted microcellular foaming with low-pressure gaseous CO2 as blowing agent. *Journal of CO2 Utilization* **53,** 101708 (Nov. 2021).

21. Guo, Q., Wang, J., Park, C. B. & Ohshima, M. A microcellular foaming simulation system with a high pressure-drop rate. *Industrial and Engineering Chemistry Research* **45,** 6153–6161. ISSN: 08885885 (2006).

22. Hu, D. *et al.* Effect of additives on the dynamic bubble growth behavior of polymer foam evaluated with in-situ visualizations and simulations. *Polymer Testing* **105,** 107419. ISSN: 01429418. https://doi.org/10.1016/j.polymertesting.2021.107419%20https://linkinghub.elsevier.com/retrieve/pii/S0142941821003627 (Jan. 2022).

23. Leung, S. N., Wong, A., Wang, L. C. & Park, C. B. Mechanism of extensional stress-induced cell formation in polymeric foaming processes with the presence of nucleating agents. *Journal of Supercritical Fluids* **63,** 187–198. ISSN: 08968446. http://dx.doi.org/10.1016/j.supflu.2011.12.018 (2012).

24. Li, R., Lee, J. H., Wang, C., Howe Mark, L. & Park, C. B. Solubility and diffusivity of CO2 and N2 in TPU and their effects on cell nucleation in batch foaming. *The Journal of Supercritical Fluids* **154,** 104623. ISSN: 08968446. https://doi.org/10.1016/j.supflu.2019.104623%20https://linkinghub.elsevier.com/retrieve/pii/S0896844619303134 (Dec. 2019).

25. Shaayegan, V., Wang, G. & Park, C. B. Study of the bubble nucleation and growth mechanisms in high-pressure foam injection molding through in-situ visualization. *European Polymer Journal* **76,** 2–13. ISSN: 00143057. http://dx.doi.org/10.1016/j.eurpolymj.2015.11.021%20https://linkinghub.elsevier.com/retrieve/pii/S001430571530063X (Mar. 2016).

26. Shaayegan, V., Wang, G. & Park, C. B. Effect of foam processing parameters on bubble nucleation and growth dynamics in high-pressure foam injection molding. *Chemical Engineering Science* **155,** 27–37. ISSN: 00092509. http://dx.doi.org/10.1016/j.ces.2016.07.040%20https://linkinghub.elsevier.com/retrieve/pii/S0009250916304158 (Nov. 2016).

27. Taki, K., Nakayama, T., Yatsuzuka, T. & Ohshima, M. Visual Observations of Batch and Continuous Foaming Processes. *Journal of Cellular Plastics* **39,** 155–169. ISSN: 0021-955X. `http://journals.sagepub.com/doi/10.1177/0021955X03039002005` (Mar. 2003).

28. Taki, K., Kitano, D. & Ohshima, M. Effect of Growing Crystalline Phase on Bubble Nucleation in Poly(L-Lactide)/CO2 Batch Foaming. *Industrial & Engineering Chemistry Research* **50,** 3247–3252. ISSN: 0888-5885. `https://pubs.acs.org/sharingguidelines%20https://pubs.acs.org/doi/10.1021/ie101637f` (Mar. 2011).

29. Wong, A. & Park, C. A visualization system for observing plastic foaming processes under shear stress. *Polymer Testing* **31,** 417–424. ISSN: 01429418. `https://linkinghub.elsevier.com/retrieve/pii/S0142941811002169` (May 2012).

30. Wong, A., Guo, Y. & Park, C. B. Fundamental mechanisms of cell nucleation in polypropylene foaming with supercritical carbon dioxideEffects of extensional stresses and crystals. *The Journal of Supercritical Fluids* **79,** 142–151. ISSN: 08968446. `http://dx.doi.org/10.1016/j.supflu.2013.02.013%20https://linkinghub.elsevier.com/retrieve/pii/S0896844613000740` (July 2013).

31. Wong, A., Wijnands, S. F. L., Kuboki, T. & Park, C. B. Mechanisms of nanoclay-enhanced plastic foaming processes: effects of nanoclay intercalation and exfoliation. *Journal of Nanoparticle Research* **15,** 1815. ISSN: 1388-0764. `http://link.springer.com/10.1007/s11051-013-1815-y` (Aug. 2013).

32. Wong, A., Mark, L. H., Hasan, M. M. & Park, C. B. The synergy of supercritical CO2 and supercritical N2 in foaming of polystyrene for cell nucleation. *Journal of Supercritical Fluids* **90,** 35–43. ISSN: 08968446. `http://dx.doi.org/10.1016/j.supflu.2014.03.001` (2014).

33. Wong, A., Guo, Y., Park, C. & Zhou, N. A Polymer Visualization System with Accurate Heating and Cooling Control and High-Speed Imaging. *International Journal of Molecular Sciences* **16,** 9196–9216. ISSN: 1422-0067. `http://www.mdpi.com/1422-0067/16/5/9196` (Apr. 2015).

34. Yang, J. *et al.* Experimental and numerical analysis of bubble nucleation in foaming polymer. *Materials & Design* **203,** 109577. ISSN: 02641275. `https://linkinghub.elsevier.com/retrieve/pii/S0264127521001301` (May 2021).

35. Pardo-Alonso, S., Solórzano, E., Estravís, S., Rodríguez-Perez, M. A. & De Saja, J. A. In situ evidence of the nanoparticle nucleating effect in polyurethane-nanoclay foamed systems. *Soft Matter* **8,** 11262–11270. ISSN: 1744683X (2012).

36. Tuladhar, T. & Mackley, M. Experimental observations and modelling relating to foaming and bubble growth from pentane loaded polystyrene melts. *Chemical Engineering Science* **59,** 5997–6014. ISSN: 00092509. https://www.sciencedirect.com/science/article/pii/S0009250904004920%20https://linkinghub.elsevier.com/retrieve/pii/S0009250904004920 (Dec. 2004).

37. Reignier, J., Alcouffe, P., Méchin, F. & Fenouillot, F. The morphology of rigid polyurethane foam matrix and its evolution with time during foaming – New insight by cryogenic scanning electron microscopy. *Journal of Colloid and Interface Science* **552,** 153–165. ISSN: 00219797. https://linkinghub.elsevier.com/retrieve/pii/S0021979719305764 (Sept. 2019).

38. Pérez-Tamarit, S., Solórzano, E., Mokso, R. & Rodríguez-Pérez, M. In-situ understanding of pore nucleation and growth in polyurethane foams by using real-time synchrotron X-ray tomography. *Polymer* **166,** 50–54. ISSN: 0032-3861. https://www.sciencedirect.com/science/article/pii/S0032386119300618 (Mar. 2019).

39. Han, J. H. & Dae Han, C. Bubble nucleation in polymeric liquids. I. Bubble nucleation in concentrated polymer solutions. *Journal of Polymer Science Part B: Polymer Physics* **28,** 711–741. ISSN: 08876266. https://onlinelibrary.wiley.com/doi/10.1002/polb.1990.090280509 (Apr. 1990).

40. Leung, S. N., Park, C. B., Xu, D., Li, H. & Fenton, R. G. Computer Simulation of Bubble-Growth Phenomena in Foaming. *Industrial & Engineering Chemistry Research* **45,** 7823–7831. ISSN: 0888-5885. https://pubs.acs.org/doi/pdf/10.1021/ie060295a%20https://pubs.acs.org/doi/10.1021/ie060295a (Nov. 2006).

41. Ando, K., Liu, A. Q. & Ohl, C. D. Homogeneous nucleation in water in microfluidic channels. *Physical Review Letters* **109,** 044501. ISSN: 00319007 (2012).

42. Tsujimura, I. *et al.* A Study of Bubble Nucleation in Foam Extrusion Die. *Seikei-Kakou* **11,** 937–944. ISSN: 1883-7417. http://www.jstage.jst.go.jp/article/seikeikakou1989/11/11/11_11_937/_article/-char/ja/ (1999).

43. Shimoda, M., Tsujimura, I., Tanigaki, M. & Ohshima, M. Polymeric foaming simulation for extrusion processes. *Journal of Cellular Plastics* **37,** 517–536. ISSN: 0021955X (2001).

44. Shaayegan, V., Mark, L. H., Tabatabaei, A. & Park, C. B. A new insight into foaming mechanisms in injection molding via a novel visualization mold. *Express Polymer Letters* **10,** 462–469. ISSN: 1788618X (2016).

45. Deveaux, S. *The Birth of Bebop* 167–236. ISBN: 9780520922105. https://www.degruyter.com/document/doi/10.1525/9780520922105/html (University of California Press, Dec. 1997).

46. Knight, J. B., Vishwanath, A., Brody, J. P. & Austin, R. H. Hydrodynamic Focusing on a Silicon Chip: Mixing Nanoliters in Microseconds. *Physical Review Letters* **80,** 3863–3866. https://journals.aps.org/prl/pdf/10.1103/PhysRevLett.80.3863 (1998).

47. Pollack, L. *et al.* Compactness of the denatured state of a fast-folding protein measured by submillisecond small-angle x-ray scattering. *Proceedings of the National Academy of Sciences* **96,** 10115–10117. ISSN: 0027-8424. http://www.pnas.org/content/pnas/96/18/10115.full.pdf%20http://www.pnas.org/cgi/doi/10.1073/pnas.96.18.10115 (Aug. 1999).

48. Squires, T. M. & Quake, S. R. Microfluidics: Fluid physics at the nanoliter scale. *Reviews of Modern Physics* **77,** 977–1026. ISSN: 00346861 (2005).

49. Brody, J. P., Yager, P., Goldstein, R. E. & Austin, R. H. Biotechnology at low Reynolds numbers. *Biophysical Journal* **71,** 3430–3441. ISSN: 00063495. http://dx.doi.org/10.1016/S0006-3495(96)79538-3 (1996).

50. Seibt, S., With, S., Bernet, A., Schmidt, H.-W. & Förster, S. Hydrogelation Kinetics Measured in a Microfluidic Device with in Situ X-ray and Fluorescence Detection. *Langmuir* **34,** 5535–5544. ISSN: 0743-7463. https://pubs.acs.org/sharingguidelines%20https://pubs.acs.org/doi/10.1021/acs.langmuir.8b00384 (May 2018).

51. Song, H. & Ismagilov, R. F. Millisecond Kinetics on a Microfluidic Chip Using Nanoliters of Reagents. *Journal of the American Chemical Society* **125,** 14613–14619. ISSN: 0002-7863. https://pubs.acs.org/doi/pdf/10.1021/ja0354566%20https://pubs.acs.org/doi/10.1021/ja0354566 (Nov. 2003).

52. Stan, C. A. *et al.* A microfluidic apparatus for the study of ice nucleation in supercooled water drops. *Lab on a Chip* **9,** 2293–2305. ISSN: 14730189 (2009).

53. Song, H., Chen, D. L. & Ismagilov, R. F. Reactions in droplets in microfluidic channels. *Angewandte Chemie - International Edition* **45,** 7336–7356. ISSN: 14337851 (2006).

54. Hassanpour-Tamrin, S., Sanati-Nezhad, A. & Sen, A. A simple and low-cost approach for irreversible bonding of polymethylmethacrylate and polydimethylsiloxane at room temperature for high-pressure hybrid microfluidics. *Scientific Reports* **11,** 4821. ISSN: 2045-2322. https://doi.org/10.1038/s41598-021-83011-8%20http://www.nature.com/articles/s41598-021-83011-8 (Dec. 2021).

55. Marre, S. & Jensen, K. F. Synthesis of micro and nanostructures in microfluidic systems. *Chemical Society Reviews* **39,** 1183. ISSN: 0306-0012. http://xlink.rsc.org/?DOI=b821324k (Feb. 2010).

56. Martin, A., Teychené, S., Camy, S. & Aubin, J. Fast and inexpensive method for the fabrication of transparent pressure-resistant microfluidic chips. *Microfluidics and Nanofluidics* **20,** 92. ISSN: 1613-4982. http://link.springer.com/10.1007/s10404-016-1757-7 (June 2016).

57. Chen, C. F. *et al.* High-pressure needle interface for thermoplastic microfluidics. *Lab Chip* **9,** 50–55. ISSN: 1473-0197. http://xlink.rsc.org/?DOI=B812812J (2009).

58. Sell, A., Fadaei, H., Kim, M. & Sinton, D. Measurement of CO 2 Diffusivity for Carbon Sequestration: A Microfluidic Approach for Reservoir-Specific Analysis. *Environmental Science & Technology* **47,** 71–78. ISSN: 0013-936X. https://pubs.acs.org/doi/10.1021/es303319q (Jan. 2013).

59. Gerhardt, R. F., Peretzki, A. J., Piendl, S. K. & Belder, D. Seamless Combination of High-Pressure Chip-HPLC and Droplet Microfluidics on an Integrated Microfluidic Glass Chip. *Analytical Chemistry* **89,** 13030–13037. ISSN: 0003-2700. https://pubs.acs.org/doi/10.1021/acs.analchem.7b04331 (Dec. 2017).

60. Utada, A. S. *et al.* Monodisperse double emulsions generated from a microcapillary device. *Science* **308,** 537–541. ISSN: 00368075 (2005).

61. Marre, S., Aymonier, C., Subra, P. & Mignard, E. Dripping to jetting transitions observed from supercritical fluid in liquid microcoflows. *Applied Physics Letters* **95,** 134105. ISSN: 0003-6951. http://aip.scitation.org/doi/10.1063/1.3242375 (Sept. 2009).

62. Roig, Y., Marre, S., Cardinal, T. & Aymonier, C. Synthesis of exciton luminescent ZnO nanocrystals using continuous supercritical microfluidics. *Angewandte Chemie - International Edition* **50,** 12071–12074. ISSN: 14337851 (2011).

63. Luther, S. K. & Braeuer, A. High-pressure microfluidics for the investigation into multi-phase systems using the supercritical fluid extraction of emulsions (SFEE). *The Journal of Supercritical Fluids* **65,** 78–86. ISSN: 08968446. https://linkinghub.elsevier.com/retrieve/pii/S0896844612000782 (May 2012).

64. Trachsel, F., Hutter, C. & von Rohr, P. R. Transparent silicon/glass microreactor for high-pressure and high-temperature reactions. *Chemical Engineering Journal* **135,** 309–316. ISSN: 13858947 (2008).

65. Temiz, Y., Lovchik, R. D., Kaigala, G. V. & Delamarche, E. Lab-on-a-chip devices: How to close and plug the lab? *Microelectronic Engineering* **132,** 156–175. ISSN: 01679317. http://dx.doi.org/10.1016/j.mee.2014.10.013%20https://linkinghub.elsevier.com/retrieve/pii/S0167931714004456 (Jan. 2015).

66. Maharrey, S. P. & Miller, D. R. Quartz capillary microreactor for studies of oxidation in supercritical water. *AIChE Journal* **47,** 1203–1211. ISSN: 00011541. http://doi.wiley.com/10.1002/aic.690470526%20https://onlinelibrary.wiley.com/doi/10.1002/aic.690470526 (May 2001).

67. Chen-Jolly, H., Guillot, P. & Mignard, E. Supercritical continuous precipitation polymerization of acrylic acid in a droplet-based millifluidic device. *Chemical Engineering Journal* **334,** 389–399. ISSN: 13858947. https://linkinghub.elsevier.com/retrieve/pii/S138589471731745X (Feb. 2018).

68. Hessberger, T. *et al.* Co-flow microfluidic synthesis of liquid crystalline actuating Janus particles. *Journal of Materials Chemistry C* **4,** 8778–8786. ISSN: 2050-7526. http://xlink.rsc.org/?DOI=C6TC03378D (Sept. 2016).

69. Khan, I. U. *et al.* Microfluidic conceived drug loaded Janus particles in side-by-side capillaries device. *International Journal of Pharmaceutics* **473,** 239–249. ISSN: 18733476. http://dx.doi.org/10.1016/j.ijpharm.2014.06.035 (2014).

70. NIST. *NIST Standard Reference Database Number 69* 2022. https://webbook.nist.gov/chemistry/ (2022).

71. Bourges, A. C., Lazarev, A., Declerck, N., Rogers, K. L. & Royer, C. A. Quantitative High-Resolution Imaging of Live Microbial Cells at High Hydrostatic Pressure. *Biophysical Journal* **118,** 2670–2679. ISSN: 15420086. https://doi.org/10.1016/j.bpj.2020.04.017 (2020).

72. Brown, P. Investigating change using the invisible-test-tube demonstration. *Science Scope* **36,** 76–81. http://www.jstor.org/stable/43184272 (2013).

73. Schnablegger, H. & Singh, Y. *The SAXS Guide: Getting acquainted with the principles* 4th ed., 50–90. ISBN: 18012013. https://austria-forum.org/web-books/en/saxs00en2013iicm/000072 (Anton Paar GmbH, Austria, Graz, Austria, 2017).

74. Steen, H. B. Flow Cytometer for Measurement of the Light Scattering of Viral and Other Submicroscopic Particles. *Cytometry Part A* **57,** 94–99. ISSN: 15524922 (2004).

75. Aschenbrenner, O. & Styring, P. Comparative study of solvent properties for carbon dioxide absorption. *Energy Environ. Sci.* **3,** 1106–1113. www.rsc.org/ees (2010).

76. Wiesmet, V., Weidner, E., Behme, S., Sadowski, G. & Arlt, W. Measurement and modelling of high-pressure phase equilibria in the systems polyethyleneglycol (PEG)–propane, PEG–nitrogen and PEG–carbon dioxide. *The Journal of Supercritical Fluids* **17,** 1–12. ISSN: 08968446 (Feb. 2000).

77. Leung, S. N., Wong, A., Park, C. B. & Guo, Q. Strategies To Estimate the Pressure Drop Threshold of Nucleation for Polystyrene Foam with Carbon Dioxide. *Industrial & Engineering Chemistry Research* **48,** 1921–1927. ISSN: 0888-5885. `https://pubs.acs.org/doi/10.1021/ie800079x` (Feb. 2009).

78. Machuga, S. C., Midje, H. L., Peanasky, J. S., Macosko, C. W. & Ranz, W. E. Microdispersive interfacial mixing in fast polymerizations. *AIChE Journal* **34,** 1057–1064. ISSN: 15475905 (1988).

79. *The Polyurethanes Book* (eds Randall, D. & Lee, S.) ISBN: 0470850418 (Huntsman International LLC, Polyurethanes business, 2002).

80. Ford, I. J. Thermodynamic properties of critical clusters from measurements of vapour–liquid homogeneous nucleation rates. *The Journal of Chemical Physics* **105,** 8324–8332. ISSN: 0021-9606. `http://aip.scitation.org/doi/10.1063/1.472687` (Nov. 1996).

81. Laaksonen, A. & Malila, J. in *Nucleation of Water: From Fundamental Science to Atmospheric and Additional Applications* 45–70 (2022).

III.S1 Flow in Microfluidic Sheath Flow

Newtonian Polyols

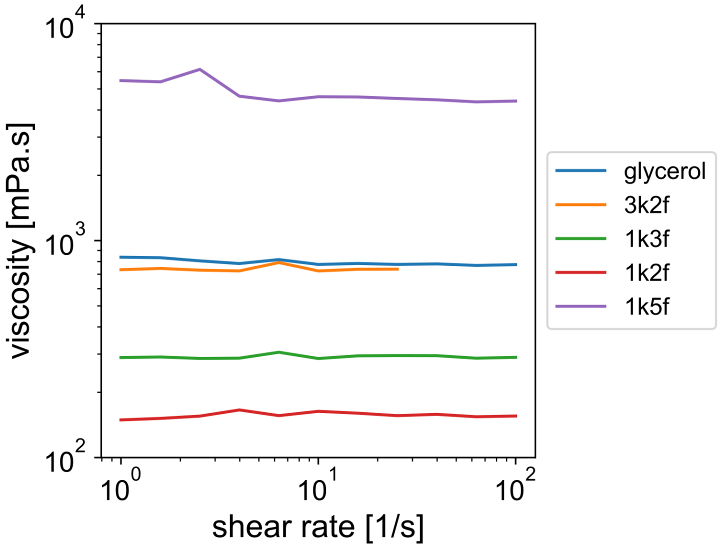

Figure III.S1: Viscosity measured in a shear rate sweep from 1 1/s to 100 1/s at a temperature of 25 degrees Celsius with 50 mm parallel plates and 0.7 mm gap size on an ARES RFS shear rheometer. Polyol names are encoded to conceal the identities of proprietary chemicals; for properties, see Table II.1.

Derivation of Flow Profile

Assumptions:

- Stokes flow ($Re \ll 1$)
- Incompressible fluid
- Newtonian fluid
- Axisymmetry about the flow axis (no θ dependence)
- Symmetric along the flow axis (no z dependence)
- Steady flow (no time dependence)
- No-slip boundary condition at the walls
- No-stress boundary condition at the interface between the inner and outer streams
- Effect of gravity is negligible

Because we assume that we are in the Stokes flow regime, the governing equation is the Stokes equation,

$$\nabla p = \eta \nabla^2 \vec{v} \tag{III.1}$$

where p is the pressure, η is the viscosity, and $\vec{v}$ is the velocity.

Because the flow is axisymmetric, there is no velocity component in the azimuthal (θ) direction. Additionally, because the flow is axisymmetric, symmetric along the flow axis, and incompressible, there is no velocity component in the radial (r) direction, either. Thus, we only need to consider the axial component of velocity (along the z-axis), which we will denote as w, according to convention. Then Stokes equation III.1 can be simplified to

$$\frac{1}{\eta}\frac{\mathrm{d}p}{\mathrm{d}z} = \frac{1}{r}\frac{\mathrm{d}}{\mathrm{d}r}\left(r\frac{\mathrm{d}w}{\mathrm{d}r}\right) \tag{III.2}$$

Because the system is translationally invariant in z, the pressure gradient is constant, $\frac{\mathrm{d}p}{\mathrm{d}z} \equiv -G$. Then the general form of the velocity profile is obtained by integrating equation III.2 twice to get

$$w = -\frac{Gr^2}{4\eta} + A\log r + B \tag{III.3}$$

However, since we are considering flow along a cylinder that includes $r = 0$ in the domain, a finite velocity requires that $A = 0$. This is true even for the outer stream's velocity profile because it may flow through $r = 0$ in the limit that the inner flow rate goes to 0.

We call the radius of the interface between the inner and outer streams R_i and the radius of the walls R. We also will denote the velocity profile of the inner stream as $w_i(r)$ on the domain $r \in [0, R_i]$ and that of the outer stream as $w_o(r)$ on the domain $r \in [R_i, R]$. Note that the inner and outer streams could have different viscosities, denoted by η_i and η_o. Because we assume no stress along the interface between the two streams, the velocity of the interface is the same on either side, which we will denote as V. Then the boundary conditions on the velocity profile $w_i(r)$ for the inner stream are

$$\begin{cases} \left.\frac{\mathrm{d}w_i}{\mathrm{d}r}\right|_{r=0} = 0, \text{(axisymmetry)} \\ w_i(r = R_i) = w_o(r = R_i) \equiv V, \text{continuous velocity} \end{cases} \tag{III.4}$$

The first boundary condition is satisfied because the coefficient of the logarithmic term $A = 0$. The second boundary condition determines the constant coefficient

$$B = V + \frac{GR_i^2}{4\eta_i} \tag{III.5}$$

Thus

$$w_i(r) = V + \frac{GR_i^2}{4\eta_i}\left[1 - \left(\frac{r}{R_i}\right)^2\right] \tag{III.6}$$

The boundary conditions on the velocity profile $w_o(r)$ for the outer stream are

$$\begin{cases} w_o(r = R_i) = V, \text{continuous velocity} \\ w_o(r = R) = 0, \text{no slip along the walls} \end{cases} \tag{III.7}$$

Solving the second boundary condition for the constant coefficient B gives

$$B = \frac{GR^2}{4\eta_o} \tag{III.8}$$

Thus, the velocity profile of the outer stream is

$$w_o(r) = \frac{GR^2}{4\eta_o}\left[1 - \left(\frac{r}{R}\right)^2\right] \tag{III.9}$$

Substituting equation III.8 into the first boundary condition gives the velocity at the interface between the inner and outer streams,

$$V = \frac{G(R^2 - R_i^2)}{4\eta_o} \tag{III.10}$$

By plugging in the expression for V from equation III.10 into the expression for the inner stream velocity profile in equation III.6, we find that the velocity profile of the inner stream is

$$w_i(r) = \frac{G(R^2 - R_i^2)}{4\eta_o} + \frac{GR_i^2}{4\eta_i}\left[1 - \left(\frac{r}{R_i}\right)^2\right] \tag{III.11}$$

The remaining unknown system parameters are the interfacial radius R_i and the negative pressure gradient G. These are set by the flow rates of the inner and outer streams, Q_i and Q_o, respectively.

Given that the inner stream's flow rate is Q_i,

$$Q_i = \int_0^{2\pi}\int_0^{R_i} w_i(r) r \mathrm{d}r \mathrm{d}\theta$$

Plugging in the result for the inner stream's velocity profile $w_i(r)$ from equation III.11 gives

$$Q_i = 2\pi \int_0^{R_i} \left\{\frac{G(R^2 - R_i^2)}{4\eta_o} + \frac{GR_i^2}{4\eta_i}\left[1 - \left(\frac{r}{R_i}\right)^2\right]\right\} r\mathrm{d}r$$
$$Q_i = 2\pi \left[\frac{G(R^2 - R_i^2)R_i^2}{8\eta_o} + \frac{GR_i^4}{16\eta_i}\right]$$

which gives the following expression for the negative pressure gradient G,

$$G = \frac{8\eta_i Q_i}{\pi R_i^2\left[2(R^2 - R_i^2)\frac{\eta_i}{\eta_o} + R_i^2\right]} \tag{III.12}$$

Next we enforce that the outer stream's flow rate be Q_o,

$$Q_o = \int_0^{2\pi}\int_{R_i}^{R} w_o(r)\, r\, \mathrm{d}r\mathrm{d}\theta$$

Plugging in the result for the outer stream's velocity profile $w_o(r)$ from equation III.9,

$$Q_o = 2\pi \int_{R_i}^{R} \left(\frac{GR^2}{4\eta_o} \left[1 - \left(\frac{r}{R} \right)^2 \right] \right) r \,\mathrm{d}r$$
$$Q_o = \frac{\pi G}{8\eta_o} \left(R^2 - R_i^2 \right)^2$$

Plugging in the result for the negative pressure gradient G from equation III.12 gives that

$$Q_o = \frac{\pi}{8\eta_o} \left(R^2 - R_i^2 \right)^2 \frac{8\eta_i Q_i}{\pi R_i^2 \left[2(R^2 - R_i^2)\frac{\eta_i}{\eta_o} + R_i^2 \right]}$$
$$Q_o = \frac{\frac{\eta_i}{\eta_o} \left(R^2 - R_i^2 \right)^2}{R_i^2 \left[2(R^2 - R_i^2)\frac{\eta_i}{\eta_o} + R_i^2 \right]} Q_i$$

Solving this equation for R_i yields four solutions. The physical solution is that for which $0 \le R_i \le R$, which is

$$R_i = R\sqrt{\frac{(Q_i + Q_o)\eta_i - \sqrt{Q_o\eta_i(Q_o\eta_i + Q_i\eta_o)}}{Q_i\eta_i + 2Q_o\eta_i - Q_o\eta_o}} \tag{III.13}$$

Based on equation III.13, we predicted the stream width for a model system of glycerol inside glycerol. We fixed the flow rate Q_{out} of the glycerol in the outer stream and varied the flow rate Q_i of the glycerol in the inner stream. For low flow rates Q_{in}, the stream width grew roughly as the square root of the inner stream flow rate, as shown in Figure III.S2. For an inner stream width of $D_{in} > 20$ μm, the Stokes flow prediction for the inner stream width is consistent with the experimental measurements within experimental uncertainty. Therefore, we conclude that the Stokes flow solution can provide a useful estimate for the inner stream radius, although its accuracy may decrease when bubbles have nucleated in the inner stream.

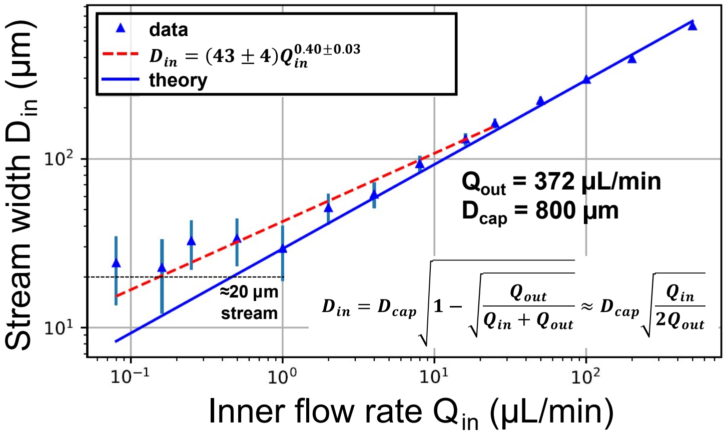

Figure III.S2: The width of the inner stream D_{in} [μm] is plotted as a function of the inner stream flow rate Q_{in} [μL/min] for an experiment flowing glycerol inside a sheath of glycerol (blue triangles with error bars indicating the experimental uncertainty in the measurement). The outer stream flow rate is fixed at Q_{out} = 372 μL/min. Based on Stokes flow of a fluid flowing inside a cylindrical shell of another fluid, the inner stream width D_{in} should follow the equation in the lower right, whose prediction is plotted (blue line) and agrees well with the measurements above 20 μm. Below 20 μm, the width of the inner stream plateaus, which could partially be the result of an optical effect. The theory simplifies to $D_{in} = D_{cap}\sqrt{\frac{Q_{in}}{Q_{out}}}$ for $Q_{in} \ll Q_{out}$, indicating that a 1/2 power-law is expected. A power-law fit is plotted (red dashed line), which has a power slightly lower than 1/2.

Lensing

Lensing is a major challenge of cylindrical capillaries. With square capillaries, lensing is eliminated because the light passes through no curved surfaces, but square capillaries and their fittings have only been shown to withstand high pressures when their dimensions are small (inner diameter of 50 μm [1]), which is not compatible with the width of the inner stream needed to prevent complete depletion of CO_2 before reaching the outlet (at least 50 μm). Lensing can occur on the inner and outer walls of the capillary, as shown in Figure III.S3. In panel (a), we show the effect of removing the lensing from the inner surface by filling the capillary with index-matched vegetable oil. In panel (b), we show the effect of removing the lensing from the outer surface by embedding the capillary in a square block of index-matched adhesive, but lensing still occurs on the inner walls, which are exposed to air. In panel (c), we show that by filling the capillary with index-matched oil and embedding it in index-matched adhesive, lensing is almost completely eliminated.

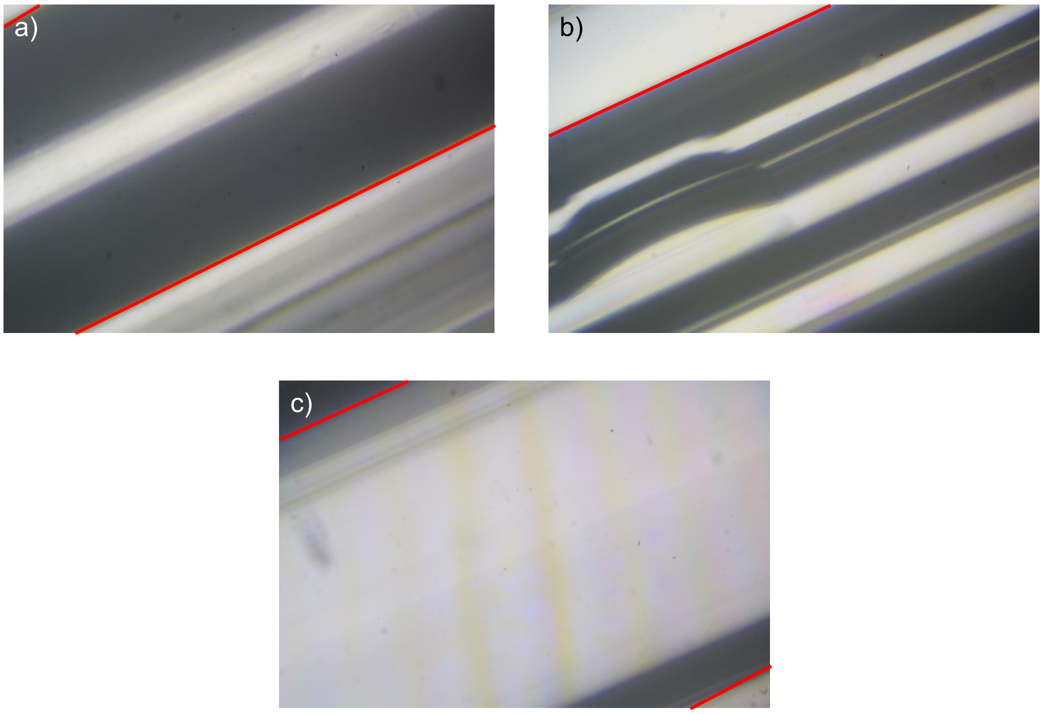

Figure III.S3: Images of borosilicate capillary (500 μm ID, 1000 μm OD) under 4x magnification with three treatments. Approximate location of inner walls of the capillary are shown with solid red lines. a) Capillary filled with index-matched oil (Wesson vegetable oil) shows lensing from a curved outer surface. b) Empty capillary embedded in square capillary filled with index-matched adhesive (146H Norland optical adhesive) shows lensing from the inner surface (slight distortion in lower right is residual oil droplet). c) Capillary filled with index-matched oil and embedded in square capillary filled with index-matched adhesive shows no lensing. Vertical streaks come from the image of the coils of the halogen light source.

III.S2 Parameter Selection

Parameter Selection

Briefly, we chose to focus on the saturation pressure of CO_2 near its critical pressure (7.39 MPa [2]) to explore the differences between supercritical and subcritical foaming. Therefore, we considered pressure quenches on the order of 10 MPa to ensure supersaturation was not reached until the fluid had traveled partway down the capillary. As discussed in Chapter IV, we ultimately focused on high-speed optical microscopy to observe bubbles. We wanted bubbles to flow at the highest speed without causing significant motion blur. The size of motion blur d_{blur} is the speed v times the exposure time τ_{exp}, $d_{blur} = v \times \tau_{exp}$. The best high-speed cameras can reach exposure times around 1 μs—shorter exposures typically are too dim to be useful. Ideally, the pixel size d_{pix} is around the diffraction limit of about

1 μm. Thus, to keep the motion blur d_{blur} smaller than the pixel size, we need $v < \frac{d_{pix}}{\tau_{exp}} \sim \frac{1\ \mu\text{m}}{1\ \mu\text{s}} \sim 1$ m/s. We chose the length of the capillary L to be roughly the length spanned by our microscope's translation stage (~ 100 mm). The residence time of the fluid in the capillary would be about $L/v \sim 100$ ms. We need the inner stream to be wide enough that it is not depleted of CO_2 before reaching the end of the observation capillary. Based on the data in Figure II.4, the maximum diffusivity we might expect is around 10^{-9} m^s/s. With that diffusivity, in 100 ms the diffusion boundary layer grows by $\sqrt{D \times t} \sim \sqrt{10^{-9}\ \text{m}^2/\text{s} \times 0.1\ \text{s}} \sim 10\ \mu$m. Therefore, the inner stream radius must be greater than 10 μm. At the same time, the inner diameter of the capillary must be small enough to maintain the $\sim 10^8$ Pa/m pressure gradient while keeping the speed of the flow below 1 m/s. In general, this requirement means that the inner stream radius must be less than 50 μm. We typically use an inner stream of 20–30 μm in radius.

We used the polyols listed in Table II.1. The most viscous polyol used was the "1k5f," which had a shear viscosity of 4820 mPa.s. Having observed that these polyols are Newtonian in the range of shear rates $\omega \in [1, 100]$ Hz, we can estimate the speed of the center of a stream of pure polyol $v_c = \frac{GR^2}{4\eta}$, where G is the pressure gradient [Pa/m], R_o is the inner radius of the capillary [m], and η is the viscosity of the fluid. As a strict upper bound, we can consider the case where the capillary is entirely filled with the most viscous polyol we will consider, which has a viscosity of about 5 Pa.s (see "1k5f" in Table II.1). The maximum inner radius of the capillary is then $R < \sqrt{\frac{4\eta v_{max}}{G}} \sim 450\ \mu$m. We ultimately considered inner radii of 100 μm, 150 μm, and 250 μm depending on the goals of the experiment. In general, we found a capillary with an inner radius of 150 μm to be most amenable to the experiments we were interested in.

To determine the wall thickness, we used the conservative form of Barlow's formula [3] to estimate the maximum pressure resistance of the capillary

$$p_{max} = \frac{2 \cdot T \cdot w}{OD} \tag{III.14}$$

where T is the tensile strength of the material [Pa], w is the wall thickness [m], and OD is the outer diameter of the capillary [m]. For tubes with a wall thickness comparable to the OD, this formula underestimates the maximum pressure resistance. Nevertheless, in case of sudden pressure spikes or imperfections in the capillary, we aimed for a pressure resistance 50% higher than the maximum pressure at which we expected to operate (10 MPa), yielding p_{max} = 15 MPa. We considered capillaries made of borosilicate (Pyrex) or made of fused quartz. While the pristine tensile strength may be measured in excess of a GPa [4], most manufacturers report a tensile strength of 7 MPa for borosilicate and 49 MPa for fused quartz. With these values, we can estimate that, to have a borosilicate capillary with an inner radius of 150 μm (ID = 300 μm) safely withstand our target pressure, *i.e.* $p_{max} > 15$ MPa, its wall thickness $w > 300$ μm. We needed to keep the wall thickness thin enough that the observation capillary could fit inside a PEEK sleeve and the PEEK sleeve could fit inside a 1/16" VICI Valco fitting, which limited the outer diameter to about 1 mm. We ultimately used a fused quartz capillary with a wall thickness of 350 μm (Molex, ID = 300 μm, OD = 1000 μm), although we successfully performed experiments at 10 MPa without incident using a borosilicate capillary with an inner diameter of 500 μm and an outer diameter of 1000 μm (Friedrich & Dimmock).

Because we observed bubbles with optical microscopy, we set the length of the observation capillary L to match that of the range of a standard microscopy translation stage ($L \approx 100$ mm). We then determined the target flow speed to be as fast as possible without introducing motion blur. For digital imaging, motion blur occurs when an object moves more than one pixel during an exposure. To prevent motion blur, the product of the speed v and exposure time τ_{exp} must be smaller than the distance spanned by one pixel d_{pix}, so $v < d_{pix}/\tau_{exp}$. As discussed in Chapter IV, videos became too dim for exposure times $\tau_{exp} < 1$ μs, and pixels corresponded to about 1 μm with the magnification we used. Therefore, we aimed to keep the speed $v < 1$ m/s. As a result, the residence time of fluid in the channel was on the order of $L/v \sim 100$ ms.

For example, as common set of parameters in an experiment would be a pressure gradient G = 10 MPa / 0.1 s = 10^8 Pa/s, an inner stream radius R_i = 20 μm, an inner stream viscosity of η_i = 0.01 Pa.s (true for polyol with 20–30 % dissolved CO_2 by mass), and an outer stream viscosity of η_o = 5 Pa.s (polyol "1k5f‘" in Table II.1), we calculate the speed along the center of the inner stream using equation III.11 for $r = 0$

$$\begin{aligned} w_i(r=0) &= G\left(\frac{(R_o^2 - R_i^2)}{4\eta_o} + \frac{R_i^2}{4\eta_i}\right) \\ &\approx 1.11 \text{ m/s} \end{aligned}$$

The predicted value of 1.11 m/s is sufficiently close to the 1 m/s desired.

For the tubing, we chose 1/16” OD because it was the smallest size for which standard high-pressure fittings and valves were available from major suppliers (*e.g.*, Valco Instruments, Swagelok). We used stainless steel because its pressure rating (10,000 psi, 69 MPa) far exceeded the pressures we considered (below 2500 psi, 17 MPa). The inner diameter was selected to be as large as possible while maintaining flexibility in the tubing—tubes with too thin of walls become inflexible. We choose Restek 1/16” stainless steel tubing with an inner diameter of 0.95 mm (measured). Finally, for the inner stream capillary, we choose the smallest stainless steel capillary available that could be silver-epoxied into this tubing, which was a CynKen 304 stainless steel tube of 0.5 mm ID × 0.8 mm OD.

III.S3 Materials for Fabrication of Flow-focusing Apparatus

We list the materials and equipment required to fabricate the flow-focusing channel shown in Figure III.3 in Table III.S1.

III.S4 High-pressure Microfluidic Flow-focusing: Device Fabrication

Machine Acrylic Tee Junction

First, we machine the 3/8”-thick acrylic block into a tee junction that can fit VICI Valco fittings. See Figure III.S4 for the dimensional drawing submitted to the machine shop.

Make Silicone Rubber Stoppers

To seal the oil or optical adhesive at the ends of the observation capillary, we use silicone rubber stoppers made in a custom mold using Smoothon Ecoflex 2-part cross-linking material. The size should match the inner dimensions of the square capillary.

Name	Quantity	Notes
Acrylic slab (3/8”-thick, at least 1” × 1”)	1	To be machined for tee junction; check for crazing and strain
VICI Valco nut and ferrule	3 ea.	Nut: Valco Instr. #ZN1S6 Ferrule: Valco Instr. #ZF1S6
1/16” stainless Swagelok nut and front and back ferrule	2 ea.	Nut: Swagelok #SS-102-1 Ferrule: Swagelok #SS-100-SET
1/16” stainless steel tubing	1 m	Restek #27768 (0.040” ID, but measured to be about 950 μm)
Stainless steel capillary (0.5 mm ID × 0.8 mm OD)	> 1 cm	CynKen #CKS1824, 304 stainless steel (for inner capillary)
Silver epoxy	Pea size	MG Chemicals 8331-A & 8331-B; Paper clip works well for mixing and spreading
Extreme-pressure PEEK tubing 1/16” OD × 0.03” ID	> 0.5 cm	McMaster Carr #51085K48; drill out ID to fit observation capillary
Quartz or Pyrex capillary	100 mm	Quartz: Polymicro Molex (300 μm × 1 mm) #1068400902 Pyrex: Friedrich & Dimmock, Inc. #B100-50-100, (500 μm × 1000 μm)
NdFeB magnets	4	8 × 8 × 8 mm
3D printer	1	for printing mount (PLA filament recommended)
Steel file	1	Useful for cutting stainless steel tubing to desired length
Diamond-pointed pen	1	To score capillaries and break to right length
20 mL scintillation vial	1	For mixing 2-part silicone rubber
Wesson vegetable oil	> 5 mL	Index of refraction (1.47) matches quartz, Pyrex, and polyol
1.5 mm-thick acrylic sheet	1	Cut to 14.5 mm × 78.5 mm for base of oil reservoir
Silicone rubber	3 pcs.	one 2 × 15 mm and two 2 × 10 mm; seals oil reservoir
Loctite epoxy	≈ 1 mL	Enough to line the acrylic base
Two-part silicone rubber	5 mL	Smoothon Ecoflex 00-50
21-gauge needle	1	For boring rubber stopper

Table III.S1: Table of materials for fabricating flow-focusing channel shown in Figure III.3.

Prepare Tubing

Next, use silver epoxy to fix the inner capillary (0.5 mm ID × 0.8 mm OD stainless steel capillary) inside the stainless steel tubing (Restek). The inner capillary

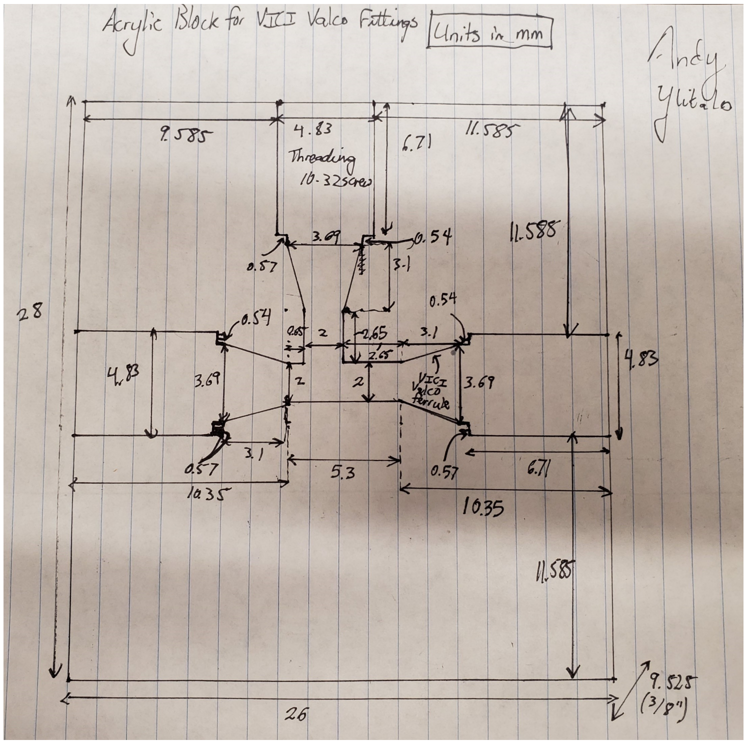

Figure III.S4: Hand-drawn dimensional sketch of acrylic tee junction to be machined from 3/8"-thick acrylic. Measurements are given in millimeters unless otherwise noted.

should extend far enough from the tubing that it clears the channel for the outer stream in the tee junction, promoting a complete and even sheath. Pump viscous polymer through the capillary before inserting it into the microfluidic apparatus to ensure that it will stay fixed under flow during experiments. The tubing should be long enough to allow for translation of the microfluidic apparatus up to 10 cm; bending the section between the ISCO pump and the apparatus into an "S" shape can provide this flexibility. The outer stream tubing is prepared similarly, but without the need for silver epoxy or as much flexibility.

Fit VICI Valco Fitting Around Observation Capillary

Next, fit a high-pressure VICI Valco fitting and PEEK sleeve onto the end of the observation capillary without breaking the capillary. The inner diameter of the PEEK sleeve may need to be bored wider with a drill to fit snugly around the observation capillary. Place the sleeve as near the end of the observation capillary as possible and thread the VICI Valco nut and ferrule over it so that a small section of the sleeve is visible beyond the end of the ferrule. Holding the pieces in their places, finger tighten into a VICI Valco fitting (HPLC fittings are suitable alternatives), then tighten with a wrench until the fitting firmly holds the capillary in place.

3D-print Microscope Stage Mount

The design for the 3D-printed mount can be found with the data that accompanies this thesis in `3_bubble_birth/device_design/mf_mount.stl`. After 3D-printing and shaving off supports, laser cut a piece of acrylic to fit into the base of the oil reservoir and epoxy in place. Test for leaks.

III.S5 Other Device Designs

As mentioned in Section III.2, we tried to reduce lensing in the observation capillary by encasing it in a UV-cured optical adhesive (Norland #146H) instead of submerging it in an oil reservoir. This method is more consistent, is cleaner, and can allow for observation nearer the exit of the observation capillary. Nevertheless, the optical adhesive is prone to entrapping small bubbles when dispensed, which obstruct imaging. Any contamination or inhomogeneities in the optical adhesive are permanently fixed upon curing, so exquisite care is necessary for this design to provide images as clear as acquired with the oil reservoir, which is much easier to adjust. Therefore, we suggest the further development of this method as future work in Section III.4. The current, unrefined method is described below to be used as a starting point for such development.

Materials

In addition to the materials required for the fabrication of the device with the oil reservoir (excepting those used for the oil reservoir), the materials listed in Table III.S2 are required to encase the observation capillary in optical adhesive.

Fabrication

Cut the two lengths of heat-shrink tubing no more than 0.5 cm. Heat-shrink the smaller around the observation capillary about 2 cm from the top of the VICI Valco nut; repeat for the larger. Thread cylindrical observation capillary through a square capillary and mount vertically. Fill with optical adhesive very slowly, being careful not to introduce bubbles. If any adhesive enters the cylindrical capillary, clean it out and start over. Mount capillary inside an airtight vacuum chamber and apply a light vacuum to remove any remaining bubbles. After, thoroughly clean any spilled adhesive and fill the square capillary as near to the top of the observation capillary as possible without allowing any to enter the capillary. Cure with UV containing 325 nm and 365 nm wavelengths.

Name	Quantity	Notes
Optical adhesive (n = 1.46)	1 mL	Norland Optical Adhesive 146H (#12-864); index-matched to polyol (1.48), pyrex (1.47), and quartz (1.46)
Square glass capillary (2.0 mm ID × 0.3 mm wall thickness)	8–8.5 cm	Friedrich and Dimmock BST-2-30
Heat-shrink tubing	2 pcs	3 mm diameter, 5 mm length; for centering observation capillary
Two-part silicone rubber stopper	1	Smoothon Ecoflex 00-50
UV-cure chamber	1	Large enough to house observation capillary when mounted vertically (Thermal Spa used for curing nail polish works)
Vacuum chamber	1	large enough to house observation capillary when mounted vertically

Table III.S2: Table of materials for encasing observation capillary in square capillary filled with index-matched optical adhesive of flow-focusing channel shown in Figure III.3.

III.S6 Other Methods Considered for Observing Early Bubble Growth

The microfluidic channel shown in Figure III.3 was originally designed for compatibility with many imaging modalities due to the possibility of observation with long exposure times. In the present work, we focused on one, high-speed optical microscopy. Here, we describe two other imaging modalities considered and explain why they were not pursued.

Small-angle X-ray Scattering (SAXS)

The earliest microfluidic flow-focusing devices were designed for use with small-angle X-ray scattering (SAXS) [5] and bubble nucleation occurs within the dimensions it probes (1–100 nm [6]). Terekhov *et al.* used SAXS to measure the size distribution of nanometer-sized helium bubbles trapped in borosilicate [7]. While the size range of SAXS is appropriate for detecting bubble nuclei, detecting bubbles in dynamic systems has not been demonstrated due to the long exposure times required (seconds). Because the instrument designed in the present study allows for continuous observation of a particular point in the foaming timeline, it allows for longer exposure times. We could then estimate an average bubble distribution by averaging the signal over time, as demonstrated for the detection of the nucleation of CO_2 particles under rapid cooling by Dingilian *et al.* [8]; additional applications of this technique were reviewed by Silva [9] and Ghazal *et al.* [10]. Furthermore, because the observation capillary can be made of fused quartz, which has a weaker background signal than borosilicate glass, the faint signal of the bubbles would not be overwhelmed by the background. The instrument is also easily portable to a beamline as long as two ISCO pumps, a Parr reactor, and gas cylinders are available. Nevertheless, we found that even a long exposure at the Advanced Photon Source at Argonne National Laboratory might not produce enough signal to detect bubble nucleation due to the low nucleation density observed and low density difference between bubble nuclei and polyol predicted.

SAXS detects differences in densities that cause small deflections of incident X-rays. Because the intensity of the signal is proportional to the square of the density difference [11], a solution of nanoparticles produces the same signal as a solution of bubbles even though nanoparticles are denser than the solvent while bubbles are less dense. We thus estimate the signal-to-noise ratio (SNR) of bubble nuclei with SAXS by measuring the signal from various concentrations of silica (SiO_2) nanoparticles in water (Nanocomposix #SISN50-25M, 50 ± 3 nm diameter) and converting to the equivalent number density of bubbles. The measurements were taken at beamline 5-ID-D of the Advanced Photon Source (APS) at the Argonne National Laboratory (Argonne, IL, USA). We pumped various dilutions of the nanoparticles into the quartz viewing cell of a Linkam stage (1.5 mm ID, 100 μm wall thickness) and scanned each concentration ten times with 3-second exposures. We repeated each measurement with deionized water to provide a background. Subtracting the background revealed a scattering signal, which is shown for different dilutions of aqueous SiO_2 nanoparticle solution in Figure III.S5. The wavelength of X-rays was 0.7293 Å and the sample–detector distance was 8.5028 m.

From Figure III.S5, we can see that the SAXS signal at 12.50 ppm of the nanoparticles follows the expected decreasing peaks and valleys of a solution of nearly monodisperse spheres (the slight polydispersity causes the valleys to be more shallow) [11]. At higher wave numbers q and lower concentrations of nanoparticles, the signal weakens and is drowned by noise, such that there is no discernible signal above the background at 0.78 ppm of nanoparticles. We want to determine the lowest weight fraction of nanoparticles that would give a discernible signal above the noise and estimate the number density of bubbles of CO_2 in polyol that would give a similar signal. If our microfluidic channel cannot produce a greater number density

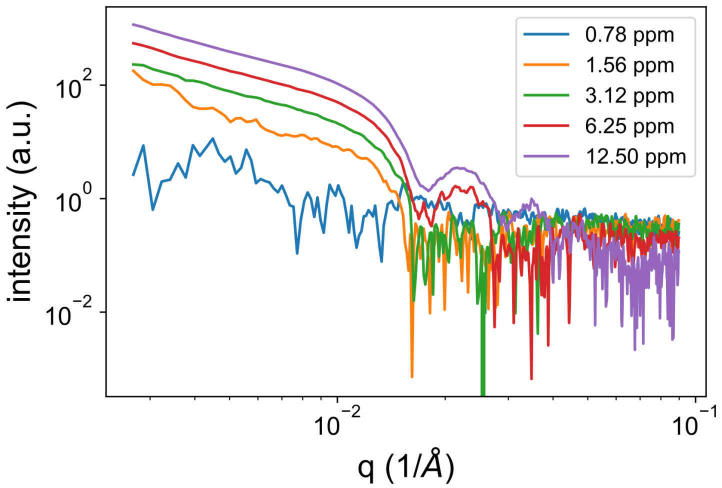

Figure III.S5: Intensity of small-angle X-ray scattering (SAXS) signal as a function of the wave number q of different concentrations of aqueous solutions of SiO_2 nanoparticles (concentrations given in ppm in legend). Signal is computed by subtracting background from water and quartz capillary. Measurements taken at beamline 5-ID-D of the Advanced Photon Source at Argonne National Laboratory (Argonne, IL, USA).

of bubbles, then we would not expect a discernible signal from bubble nucleation using SAXS.

To estimate the noise in the signal, we compute the statistical uncertainty in the signal computed by subtracting the background (water) from a scan (water and nanoparticles) σ_{signal}. We estimate this uncertainty by adding the standard deviation in the intensity of scans of water and nanoparticles (signal + background) σ_{scan} to the standard deviation in the intensity of scans of water (background) σ_{bkgd} in quadrature, $\sigma_{signal} = \sqrt{\sigma_{scan}^2 + \sigma_{bkgd}^2}$. Because the background drifts much more than the statistical uncertainty over the course of experiments (1 hour), as shown in Figure III.S6, we isolate the statistical uncertainty by computing the standard deviation of sets of ten consecutive scans and then averaging across each set of non-consecutive scans. This drift prevents the reduction in the noise level by averaging over more consecutive scans.

We compare our estimate for the statistical uncertainty to the background-subtracted signal of an aqueous solution of 1.6 ppm SiO_2 nanoparticles and the background signal in Figure III.S7. The signal-to-noise ratio (SNR) is roughly largest near the forward scattering peak $I(q = 0)$, where the signal is about 3.4 times larger than the noise $I(q = 0) \approx 3.4\sigma_{bkgd}(q = 0)$. We would therefore expect

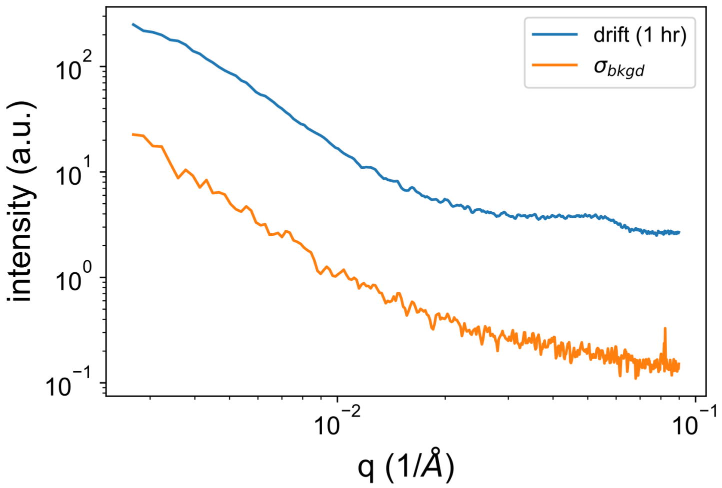

Figure III.S6: Comparison of drift in background signal (water and quartz capillary) over 1 hour and the standard deviation within ten consecutive background scans for scans shown in Figure III.S5.

no discernible signal at concentrations below 1.6 ppm / 3.4 ≈ 0.5 ppm. Indeed, we see in Figure III.S5 that while the signal at 1.56 ppm (orange) is discernible at low q values, the signal at 0.78 ppm is indistinguishable (blue) from the background, suggesting that our estimate of a discernible signal at 0.5 ppm is low.

Using 0.5 ppm as our estimate of the lowest concentration of SiO_2 nanoparticles that produce a SAXS signal discernible above the noise, we will estimate the number density of CO_2 bubbles in a polyol–CO_2 mixture that would produce a similar signal. Although we will show a model in Chapter VI that predicts bubbles nucleate with a diameter around 5–10 nm, these nuclei are much smaller and denser, so they will produce a significantly weaker SAXS signal than 50 nm bubbles; if we cannot detect a signal from 50 nm bubbles, neither will we detect a signal from bubble nuclei. For a fixed beam intensity, the forward scattering $I(q = 0)$ is proportional to the square of the total excess scattering length of a particle and the number density of particles. The total excess scattering length scales with the square of the product of the difference between the densities of the particles and the solvent $\Delta\rho = \rho_{part} - \rho_{solv}$ and the volume of each particle V [11]. Thus, the forward scattering $I(q = 0) \propto (\Delta\rho V)^2 n$. For $I(q = 0)$ to be equal for a solution of SiO_2 nanoparticles and a solution of bubbles,

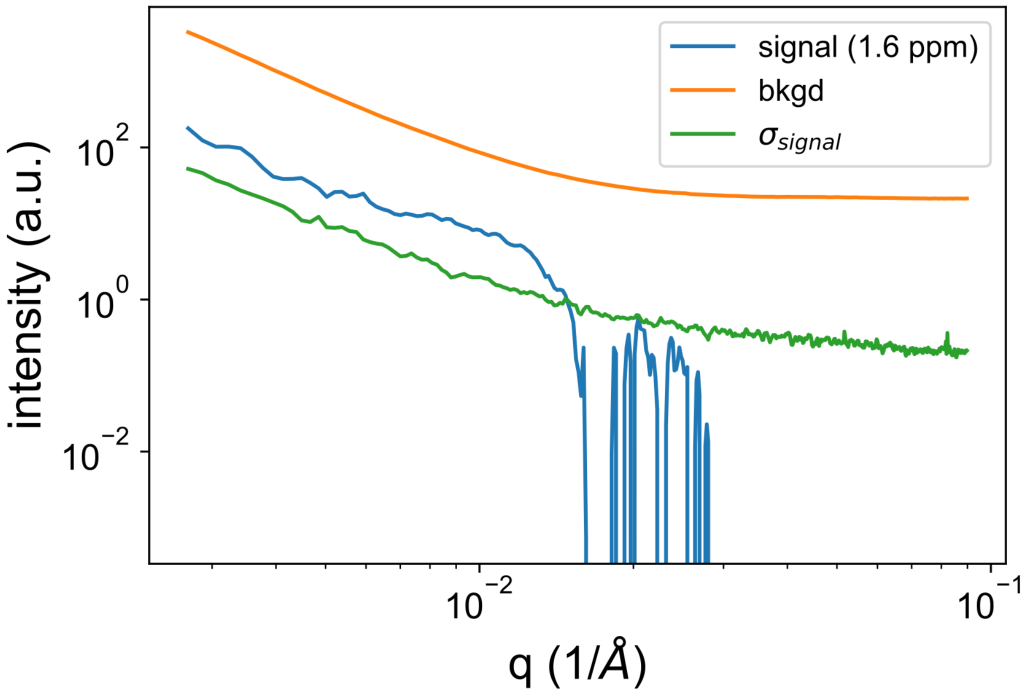

Figure III.S7: Comparison of small-angle X-ray scattering (SAXS) signal (blue) of a 1.6 ppm aqueous solution of 50 nm SiO_2 nanoparticles, the background (water and quartz capillary; orange), and the statistical uncertainty in the signal (σ_{signal}). Note that the signal becomes featureless when its intensity decreases below the statistical uncertainty.

$$I_{SiO2}(q = 0) = I_{bub}(q = 0)$$
$$(\Delta\rho_{SiO2}V_{SiO2})^2 n_{SiO2} = (\Delta\rho_{bub}V_{bub})^2 n_{bub}$$

Assuming bubbles of 50 nm in diameter, $V_{SiO2} = V_{bub}$, so

$$n_{bub}^{equiv} = \left(\frac{\Delta\rho_{SiO2}}{\Delta\rho_{bub}}\right)^2 n_{SiO2} \tag{III.15}$$

where $\Delta\rho_{SiO2} = \rho_{SiO2} - \rho_{H2O}$ and $\Delta\rho_{bub} = \rho_{CO2} - \rho_{poly}$. The densities of SiO_2 and H_2O are known to be $\rho_{SiO2} = 2.26$ g/mL and $\rho_{H2O} = 1.0$ g/mL, respectively. While our predictions suggest that CO_2 bubbles nucleate with a liquid-like density (see Figure VI.4), by the time they have grown from their initial size of around 10 nm to 50 nm, we estimate that the density of CO_2 inside would decrease to about $\rho_{CO2} \approx 0.1$ g/mL (see predictions of bubble growth model in Figure V.7). Finally, the density of polyol–CO_2 mixtures remain around $\rho_{poly} \approx 1.0$ g/mL based on the

G-ADSA measurements reported in Section II.2. Plugging in these values gives the relationship

$$n_{bub}^{equiv} \approx 2n_{SiO2} \tag{III.16}$$

indicating that twice as many 50-nm bubbles of CO_2 in polyol as 50-nm SiO_2 nanoparticles in water are needed to generate the same SAXS intensity. In some cases, we expect the bubble to nucleate with a liquid-like density (see Chapter VII). If the density remains liquid-like when the bubble has grown to tens of nanometers, the signal will be much weaker than predicted in the following analysis as a result of the squared dependence on the difference in density from the solvent.

The concentration of SiO_2 nanoparticles in the aqueous solution was given in a parts per million weight fraction w_{SiO2}. Because of the low concentration, the density of the solution is roughly that of water, 1.0 g/mL, so the weight fraction in [g SiO_2 /g solution] is equivalent to the weight fraction in [g SiO_2 / mL solution]. Each SiO_2 nanoparticle has a mass of $m_{SiO2} = \rho_{SiO2}\left(\frac{4}{3}\pi R_{SiO2}^3\right) \approx 1.5 \times 10^{-10}$ μg, where $R_{SiO2} = 25$ nm is the radius of a nanoparticle. The number density of nanoparticles is therefore $n_{SiO2} = w_{SiO2}/m_{SiO2}$, for w_{SiO2} in ppm and m_{SiO2} in μg. Thus,

$$n_{bub}^{equiv} \approx \frac{2}{1.5 \times 10^{-10}\ \mu\text{g}} w_{SiO2} \tag{III.17}$$

We determined above that the lowest weight fraction of SiO_2 nanoparticles with a discernible signal is $w_{SiO2} \approx 0.5$ ppm, so the equivalent number density of bubbles is $n_{bub}^{equiv} \approx \frac{2}{1.5\times10^{-10}} \times 0.5$ bubbles/ mL $\approx 6 \times 10^9$ bubbles / cm^3. This density is equivalent to a lattice of bubbles separated by a distance of $(n_{bub}^{equiv})^{-1/3}$ cm ≈ 5.5 μm. Given that the closest we have observed bubbles nucleate is on the order of 10 μm (see Figure V.7) and that most of the observation capillary is filled with pure polymer, we concluded that our experimental method does not nucleate enough bubbles to be detected by SAXS at 50 nm diameter, let alone at 5–10 nm upon nucleation.

Light Scattering

Light scattering is another technique known for its ability to detect and measure the size of sub-micron objects [12], including bubbles [13]. Mie scattering of droplets of polyol supersaturated with CO_2 was explored as a complementary method for detecting bubble nucleation by Laccetti, although further work remains to generate droplets from high-viscosity liquids, generate droplets with dissolved gas, and generate droplets while maintaining high pressure [14]. Light scattering could also be applied to the instrument presented in Figure III.3. While a laser could be coupled into the inner stream from upstream, such as through an optical window inserted into a bored hole in a 90° elbow junction, the laser would leak out of the inner stream upon ensheathing due to the higher index of refraction of the outer stream, leading to attenuation of the signal before reaching a bubble—see the schematic in Figure III.S8. Alternatively, a plane-wave laser could be directed along the length of the observation capillary and observed with a wide-angle camera to detect early nucleation events along the capillary.

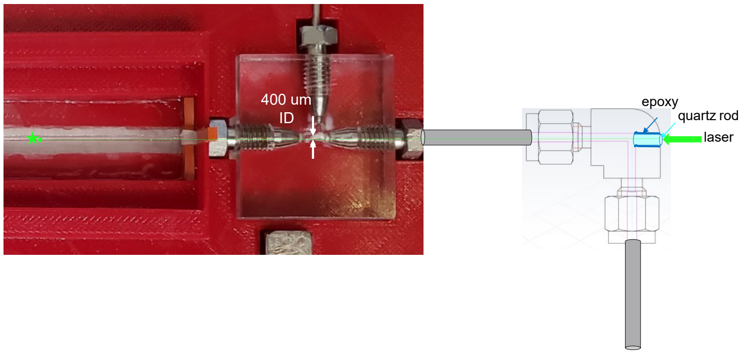

Figure III.S8: Schematic of an idea for laser scattering. A laser (green) could be coupled into an epoxied quartz rod aligned inside a 90° Swagelok elbow joint aligned along the inner stream tubing and observation capillary. The alignment is critical because the inner stream has a lower index of refraction than the outer stream due to the dissolved CO_2, so a laser signal will attenuate as it passes along it. If the alignment is precise, as could be achieved with an optical bench, the laser could be scattered by nanoscopic nuclei almost as soon as they nucleate along the observation capillary and the locations recorded with a wide-angle camera lens.

We anticipate that the most feasible application of light scattering would involve the focus of a laser directed perpendicularly to the observation capillary at a precise point along its length, ideally with a spot size less than 1 mm. While the matching of the indices of refraction of the outer stream, quartz observation capillary, and oil reservoir eliminates most lensing effects, the difference in index of refraction between the inner and outer streams due to the presence of high concentrations of dissolved gas or other additives (Chapter VII) in the inner stream would distort the background scattering. The detection of a bubble would therefore require that the signal from the bubble is distinguishable from these distortions as well as the fluctations therein caused by disturbances in the inner stream. We have not implemented this method, but offer it as a suggestion for future work.

References

1. Bourges, A. C., Lazarev, A., Declerck, N., Rogers, K. L. & Royer, C. A. Quantitative High-Resolution Imaging of Live Microbial Cells at High Hydrostatic Pressure. *Biophysical Journal* **118,** 2670–2679. ISSN: 15420086. https://doi.org/10.1016/j.bpj.2020.04.017 (2020).

2. NIST. *NIST Standard Reference Database Number 69* 2022. https://webbook.nist.gov/chemistry/ (2022).

3. Adams, A. J., Grundy, K. C., Kelly, C. M., Lin, B. & Moore, P. W. *The Barlow Equation for Tubular Burst: A Muddled History* in *IADC/SPE Drilling Conference and Exhibition* (SPE, Forth Worth, TX, USA, Mar. 2018). https://onepetro.org/SPEDC/proceedings/18DC/3-18DC/Fort%20Worth,%20Texas,%20USA/214112.

4. Holmquist, T. J. & Wereszczak, A. A. The Internal Tensile Strength of a Borosilicate Glass Determined from Laser Shock Experiments and Computational Analysis. *International Journal of Applied Glass Science* **5,** 345–352. ISSN: 20411286. https://onlinelibrary.wiley.com/doi/10.1111/ijag.12097 (Dec. 2014).

5. Pollack, L. *et al.* Compactness of the denatured state of a fast-folding protein measured by submillisecond small-angle x-ray scattering. *Proceedings of the National Academy of Sciences* **96,** 10115–10117. ISSN: 0027-8424. http://www.pnas.org/content/pnas/96/18/10115.full.pdf%20http://www.pnas.org/cgi/doi/10.1073/pnas.96.18.10115 (Aug. 1999).

6. Schnablegger, H. & Singh, Y. *The SAXS Guide: Getting acquainted with the principles* 4th ed., 50–90. ISBN: 18012013. https://austria-forum.org/web-books/en/saxs00en2013iicm/000072 (Anton Paar GmbH, Austria, Graz, Austria, 2017).

7. Terekhov, A. Y. *et al.* Small-angle X-ray scattering measurements of helium-bubble formation in borosilicate glass. *Journal of Applied Crystallography* **39,** 647–651. ISSN: 0021-8898. http://scripts.iucr.org/cgi-bin/paper?S0021889806025672 (Oct. 2006).

8. Dingilian, K. K. *et al.* Homogeneous nucleation of carbon dioxide in supersonic nozzles I: Experiments and classical theories. *Physical Chemistry Chemical Physics* **22,** 19282–19298. ISSN: 14639076 (2020).

9. Silva, B. F. B. SAXS on a chip: from dynamics of phase transitions to alignment phenomena at interfaces studied with microfluidic devices. *Physical Chemistry Chemical Physics* **19,** 23690–23703. ISSN: 1463-9076. http://xlink.rsc.org/?DOI=C7CP02736B (Sept. 2017).

10. Ghazal, A. *et al.* Recent advances in X-ray compatible microfluidics for applications in soft materials and life sciences. *Lab on a Chip* **16,** 4263–4295. ISSN: 1473-0197. http://xlink.rsc.org/?DOI=C6LC00888G (Nov. 2016).
11. Svergun, D. I. & Koch, M. H. J. Small-angle scattering studies of biological macromolecules in solution. *Reports on Progress in Physics* **66,** 1735–1782. ISSN: 0034-4885. http://stacks.iop.org/0034-4885/66/i=10/a=R05?key=crossref.536fbea0624dc0240270c53faac55ce5 (Oct. 2003).
12. Stetefeld, J., McKenna, S. A. & Patel, T. R. Dynamic light scattering: a practical guide and applications in biomedical sciences. *Biophysical Reviews* **8,** 409–427. ISSN: 18672469. http://dx.doi.org/10.1007/s12551-016-0218-6 (2016).
13. Han, J. H. & Dae Han, C. Bubble nucleation in polymeric liquids. I. Bubble nucleation in concentrated polymer solutions. *Journal of Polymer Science Part B: Polymer Physics* **28,** 711–741. ISSN: 08876266. https://onlinelibrary.wiley.com/doi/10.1002/polb.1990.090280509 (Apr. 1990).
14. Laccetti, B. J. *Therapeutic Microparticles and Biolistic Drug-Delivery to the Cornea* PhD thesis (California Institute of Technology, 2020). https://resolver.caltech.edu/CaltechTHESIS:10182020-133113205.